UNIVERSITY OF OKLAHOMA

GRADUATE COLLEGE

INVESTIGATION OF TRIPLY PERIODIC MINIMAL SURFACES IN COMPARISON TO HONEYCOMB FOR AEROSPACE APPLICATION

A THESIS

SUBMITTED TO THE GRADUATE FACULTY

In partial fulfillment of the requirements for the

Degree of

MASTER OF SCIENCE

By

JULIA WAGNER

Norman, Oklahoma

2025

INVESTIGATION OF TRIPLY PERIODIC MINIMAL SURFACES IN COMPARISON TO HONEYCOMB FOR AEROSPACE APPLICATION

A THESIS APPROVED FOR THE

SCHOOL OF AEROSPACE AND MECHANICAL ENGINEERING

BY THE COMMITTEE CONSISTING OF

Dr. Yingtao Liu, Chair

Dr. Christopher Billings, Co-Chair

Dr. Jivtesh Garg

Acknowledgements

I would like to start by thanking Dr. Yingtao Liu for all his support and advice for the past two years. I would not have been able to produce these results without his expert engineering guidance as I learned more about the research process. I must thank him for his suggestions during all my weekly presentations to ensure my research was headed in the right direction, as well as being a patient and kind advisor.

Next, I would like to thank Dr. Christopher Billings for his time and assistance in the manufacturing of the stainless-steel samples. I would also like to thank him and Dr. Jivtesh Garg for their expertise as members of my thesis committee.

I would like to extend my thanks to Dr. Ramkumar Parthasarathy who has been a constant support in my academic career. His dedication to all the AME students was a large reason I chose to study at OU. With his advance, I was able to find research that related to my career interests. I cannot thank him enough for his support throughout my time at OU.

Thank you to Joshua Hall for teaching me how to operate the Instron and the DIC. I would not have been able to obtain such clear results without his guidance. Thank you to Peter Vu for teaching me how to use the SLA printer and helping me with any troubleshooting issues. Thank you to Wilson Smith and Avery Melster for helping print any supporting materials from the PLA printers. Thank you to my colleagues at OU for being there to offer support and talk through ideas when I was having trouble figuring out an issue. I will always be grateful for the support my colleagues have provided.

Finally, I cannot thank my family enough for all the support I received while at OU. Thank you so much to my mom and my dad for always listening to me, encouraging me, and for teaching me everything I know. Thank you to my fiancé, James Kircus, for providing constant support through the ups and downs, listening to all my research ideas, and telling me which ones were good and bad. Thank you to all my friends at OU. I could not ask for better support than what has been provided by my family and friends.

Table of Contents

Table of Figures

Table of Tables

Abstract

Optimizing structures into a lattice can lead to efficient designs with highly desired properties. In aerospace applications, Honeycomb lattice structures are used for lightweighting purposes. Honeycomb is easy to manufacture out of a variety of materials but has anisotropic properties. Due to this, other types of cores for sandwich composites could be used investigated for lightweighting purposes. Triply Periodic Minimal Surfaces (TPMS) are structures that can only be manufactured using 3D printing. The Gyroid, Schwarz Primitive (Primitive) and Schwarz Diamond (Diamond) lattice structures were chosen to compare to Honeycomb for aerospace applications due to their isotropic nature. The models were parameterized in SolidWorks and evaluated in Ansys. The Diamond lattice was eliminated for comparison in the simulation process. The SLA printing process was chosen as the material to compare the remaining samples due to its high-resolution capabilities. Each sample was evaluated in compression and was tested five times and averaged for statistical significance. Honeycomb was tested in two directions due to the anisotropic property. Both the Axial and Transverse directions were tested five times and averaged for statically significance. The compression strength of each lattice was normalized by the average sample density. The results show the Gyroid with a strength-to-density of 5.692, the Primitive with a ratio of 5.182, the Honeycomb Axial with a ratio of 26.144, and the Honeycomb Transverse with a ratio of 1.008, all in $\frac{N}{\frac{kg}{m^3}}$. These results clearly indicate that Honeycomb is best in the axial direction when uniaxially loaded. For other applications where the load paths vary in multiple directions, such as a truss on a truss-braced wing, the Gyroid may be a better option due to the isotropic nature of the structure.

Chapter 1: Introduction

1.1 Benefits of Lattice Structures

Lightweight structures are necessary for efficient designs due to the ability to reduce structural weight while maintaining strength. This can be seen in buildings that use trusses, I-beams, and other shapes to increase rigidity while eliminating the unnecessary material [1]. Lightweight structures can also increase fuel efficiency in automobiles and aircraft by decreasing the energy needed to move the structure. Furthermore, lightweight structures use less material [2]. Many new methods to implement lightweight structures are continually investigated. One method to decrease the weight of a structure is by organizing the material into a lattice structure.

A lattice structure is a porous shape that repeats itself in three directions to form a larger structure. These structures have highly desired properties such as decreased weight, high strength, energy absorption, heat dissipation and vibration reduction [3]. This means the implementation of lattice structures to current designs can benefit construction and transportation in a multitude of ways.

A common real-world example of a lattice structure is hexagonal Honeycomb. Honeycombs can be seen in bee hives to maximize the storage space for honey while using the smallest amount of wax to build the structure [4]. These structures are strong enough to hold the honey, while maintaining structural integrity. This lattice structure has been used for many applications and may be an efficient way to lightweight structures. Specifically for aerospace applications, Honeycomb is commonly used as a sandwich composite to increase thickness and rigidity in structures.

1.2 Honeycomb Sandwich Composites Overview

Honeycomb sandwich composites are structures used for lightweighting in aerospace applications. These structures, generally used as sandwich structures between composite laminates to increase rigidity and strength. They are also easy to manufacture and increase the strength of the laminate without adding much weight. Honeycomb sandwich structures are used for aircraft control surfaces, such as the wingtips, fin, rudder, elevators and/or ailerons, as well as aircraft and engine nacelles, engine doors, and landing gear applications [5], [6]. For spacecraft, Honeycomb can be used for pyroshock isolation in booster separation or payload fairing on the launch vehicle, but are not as widely used due to the load loading conditions and temperature gradient present during takeoff [7], [8]. An example of these common applications is shown in Figure 1. Notice that the load path on the control surfaces on aircraft leads to compressive forces on the Honeycomb core.

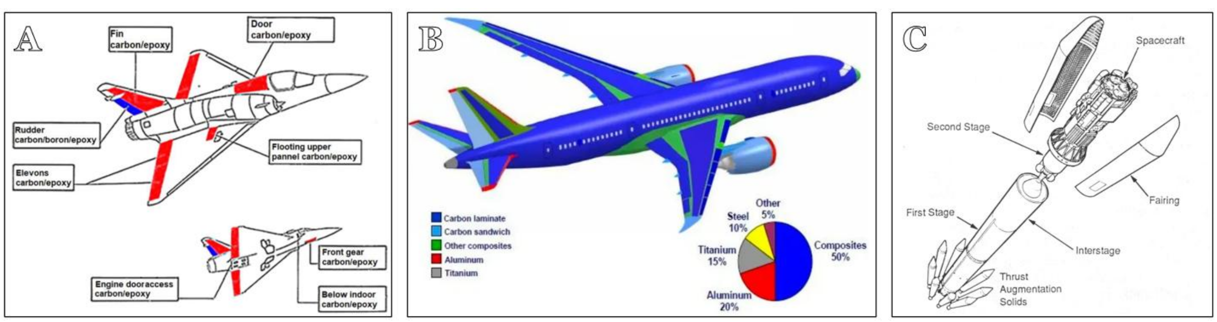

Figure 1: Honeycomb Composites used in (a) F1 aircraft [5], (b) Boeing 787 aircraft [6], and (c) rocket payload fairings [8]

Honeycomb core is made using several different materials. For aerospace applications, Nomex and aluminum are the most popular options [9]. The structure is manufactured using the expansion process. As seen in Figure 2, the expansion process started with a flat sheet of material. Bonding lines are added to the structure. Another sheet is laid on top of the structure at the proper angle. This process continues until a compressed Honeycomb sheet has been made. The sheet is then expanded into a Honeycomb core.

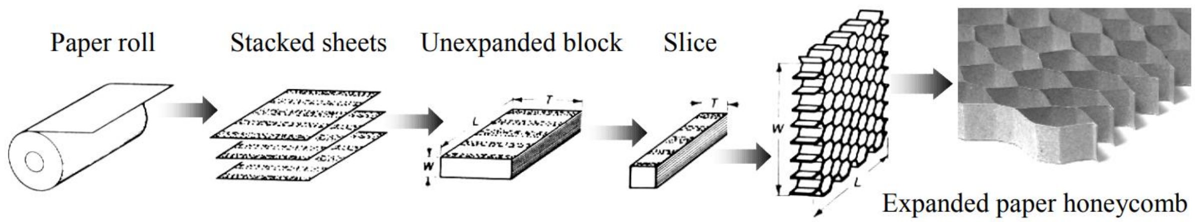

Figure 2: Honeycomb Expansion Manufacturing Process [10]

There are many potential manufacturing methods for laminated composites. Some of these manufacturing methods include a hand layup, prepreg method, press method, vacuum bagging in an autoclave method, resin infusion, resin transfer molding, compression molding, etc. The core is bonded to the carbon fiber using epoxy resin. [5]. An example of a Honeycomb sandwich composite used in industry is shown in Figure 3.

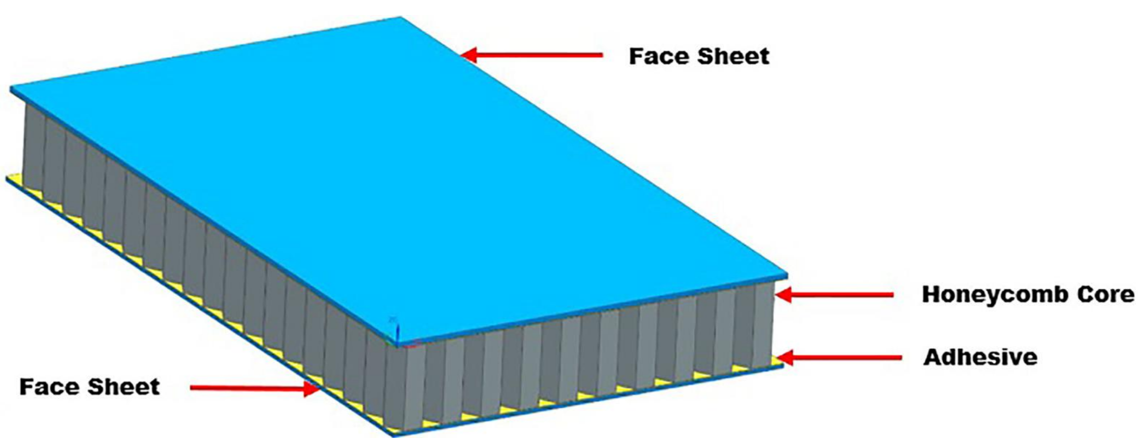

Figure 3: Honeycomb Sandwich Structure [5]

Laminated composites are typically paired with Honeycomb core to increase rigidity of structures. Carbon fiber is a common composite used in this application. Laminated carbon fiber composites are commonly made of long strands that are weaved together in opposite directions. These different orientations of the woven fiber cause it to respond to load in the most optimized way. Axial loading is when the load is applied parallel to the fiber. This is the strongest orientation. Transverse loading is the weakest loading orientation, when the load is applied perpendicular to the fiber. Figure 4 shows an example of these orientations. Fibers can be oriented in such a way that the load direction affects the part evenly. This is commonly done by laying the plies in 0-, 45-, and 90-degree orientation, also shown in Figure 4. Due to the naming convention used in laminated composites, the same terminology will be used for Honeycomb. An example of the terminology for Honeycomb is given in Figure 5.

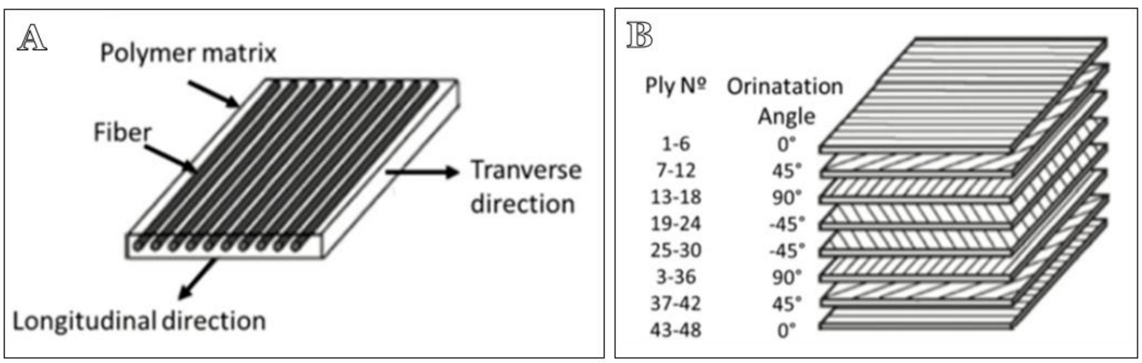

Figure 4: Composite (a) Loading Directions and (b) Ply Applications [11]

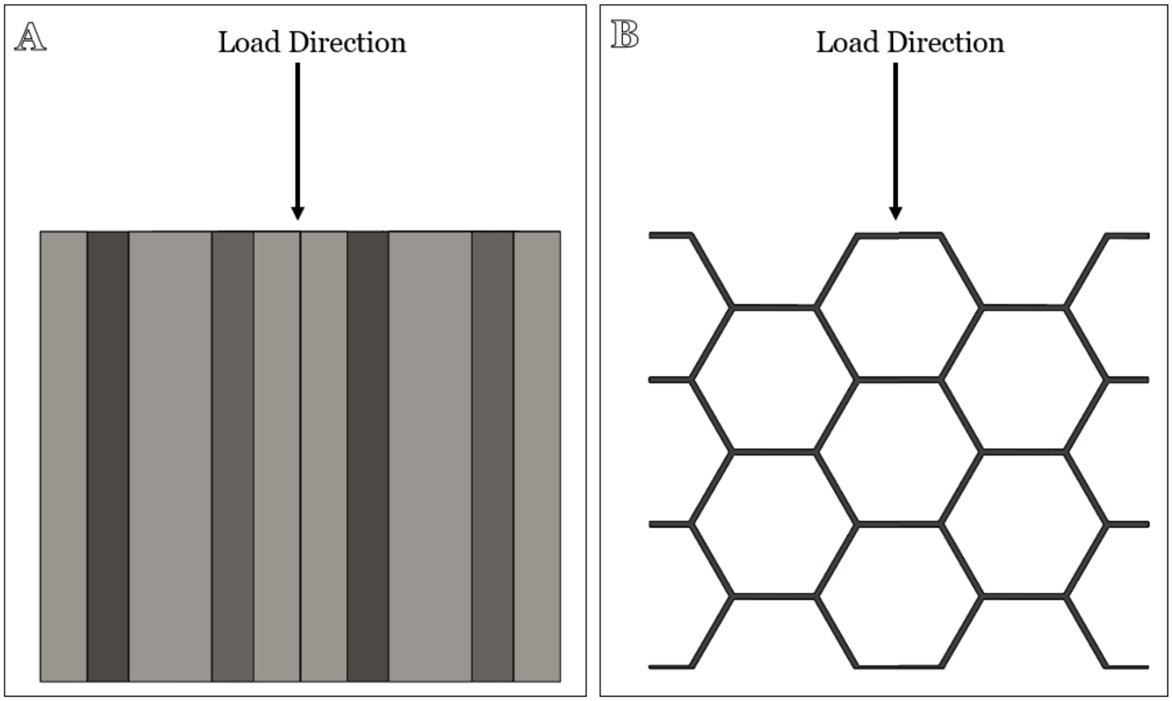

Figure 5: Honeycomb Nomenclature (a) Axial and (b) Transverse

Honeycomb itself is strong in the axial direction, but weak in the transverse direction. In other words, the isotropic property of the material used is lost when it is organized into Honeycomb lattice structure. There is little research on the response of out-of-plane loading to Honeycomb structures, meaning it is used only for in-plane loading conditions [12]. This anisotropic behavior can cause a need for more advanced analysis in the case of oblique loading.

There are many applications for multi-directional loading in aerospace engineering. For example, truss-braced wings are a rising design consideration in the aerospace industry. Wing trusses experience loading in multiple directions as the wing deflection changes, shown in Figure 6 [13]. Honeycomb is not an appropriate consideration for this type of structure, meaning aluminum ribs must be used to account for the loading directions [14]. Another type of lattice structure would be needed for this application.

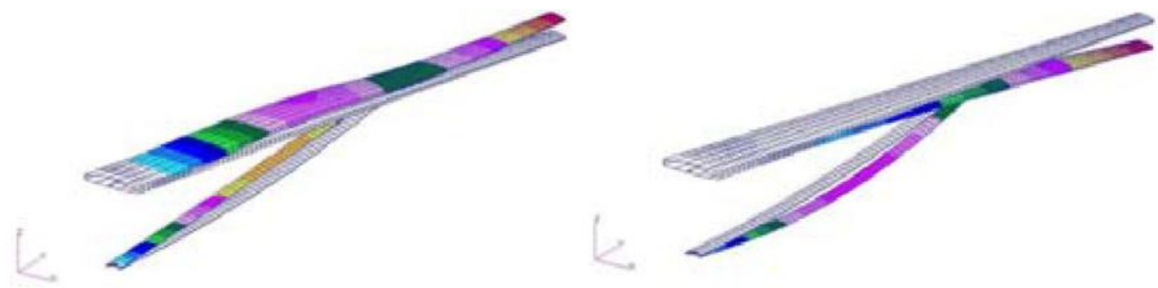

Figure 6: Common Deflection in a Truss-Braced Wing [13]

Additionally, many industries in aerospace engineering insert additional material into the Honeycomb filler material to enhance the strength of the Honeycomb [5]. This adds weight to a structure that was made for the purpose of weight reduction. Moreover, a common high-speed aircraft phenomenon, wing flutter, is dependent on an interaction between stiffness, mass properties, and aerodynamic forces. There are studies that show the thickness of Honeycomb within sandwich composites can change flutter properties [15]. While the anisotropic Honeycomb lattice would not be applicable due to the nonlinear nature of flutter, isotropic lattice structures could be a more effective way to change flutter characteristics. Furthermore, control surfaces of the wing could be more rigid in all directions with applications of isotropic lattice structures instead of Honeycomb filler. Due to this disadvantage of Honeycomb's anisotropic behavior, there is a need for an investigation of isotropic structures for aerospace applications that may reduce weight without the need for filler material.

1.3 Isotropic Lattice Structure Investigation

Lattice structures, such as Honeycomb, are used to reduce weight in a structure while keeping the structural integrity intact. Honeycomb, while popular for aerospace applications, is anisotropic. For multi-directional load applications, it may not be a viable option. Isotropic properties also reduce computations in numerical analysis, as the lattice can be treated as a lightweight isotropic material in several different types of analysis. Due to this, multiple other isotropic lattice structures were considered for aerospace applications.

First, the simplest of isotropic structures were considered: Simple Cubic (SC), Body Centered Cubic (BCC), and Face Centered Cubic (FCC). These lattices are made using a cube structure (SC), and either adding struts to the central body (BCC), or adding struts to each face (FCC), shown in Figure 7. These lattice structures were chosen for initial investigation due to their simplicity to model and understand. The models are easy to adjust by size and thickness. However, the SC lattice has extremely low packing efficiency and both the SC and FCC lattice are often subject to structure dislocations [16], [17]. Finally, the BCC lattice can see anisotropic properties, which would automatically eliminate this shape for an isotropic comparison [18]. After brief consideration, it was decided that further investigation of different structures was needed.

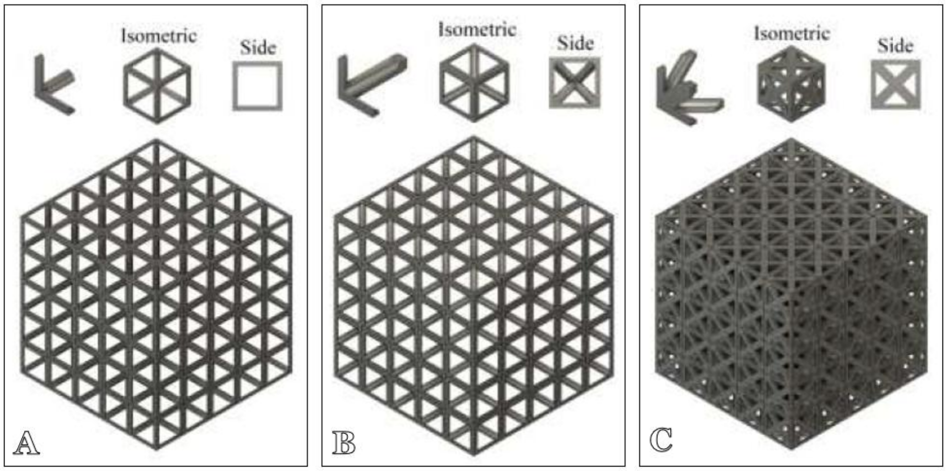

Figure 7: (a) SC, (b) BCC, and (c) FCC Lattice Structures [19]

Next, lattice structures using a sheet or surface were investigated to find a better comparison to Honeycomb. Triply Periodic Minimal Surfaces (TPMS) were the next isotropic candidate for comparison to Honeycomb for aerospace applications [20]. Triply Periodic Minimal Surfaces have reached their name for several reasons. First, a surface is considered 'triply periodic' if it repeats itself in three directions, creating a pattern in 3D space. This is the basis of a lattice structure. Moreover, it is minimal if the mean curvature of the surface is equal to zero [21]. And finally, surface refers to mathematical language that describes these structures due to their lack of thickness in the theorical world.

Originally derived from mathematics, TPMS were first proposed first by Euler, answering the prompt "Given a closed curve C, determine a connected surface S bounded by the curve, so that the area of S is a minimum', which was found later by Mousier to be TPMS [22]. Schwarz did an investigation of the creation of TPMS and created some of the most well-known TPMS today, namely, the Schwarz Primitive, Schwarz Diamond, and Schwarz Hexagonal shapes named after him. When properly oriented, these shapes form a lattice structure using sheets of material. Two of the Schwarz lattices, along with the popular Gyroid structure, are shown in Figure 8.

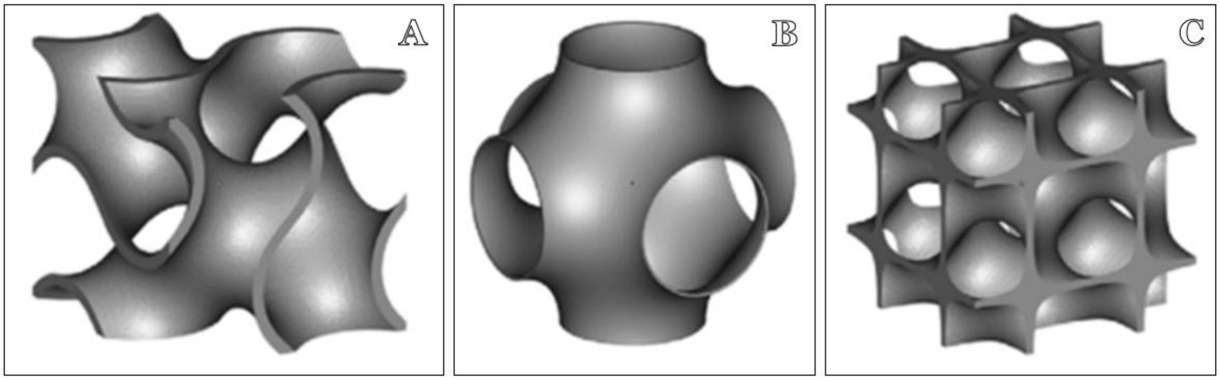

Figure 8: (a) Gyroid, (b) Primitive, (c) Diamond TPMS [23]

One advantage of TPMS is that they are a phenomenon seen in many different places in nature on a microscopic level. The most common TPMS seen in nature are the Primitive, Diamond, and Gyroid surfaces. The development of butterfly wings uses a process of degradation that ends with the most optimized structure as a Gyroid, and a beetle skeleton uses the Diamond structure for its reflective properties, shown in Figure 9 [24]. These structures provide the baseline for nature's own lightweighting lattices for enhanced strength-to-weight ratio. Another advantage of the TPMS is that they allow stress effective geometry. This is due to lack of corners and intersections that cause stress concentrations in other structures.

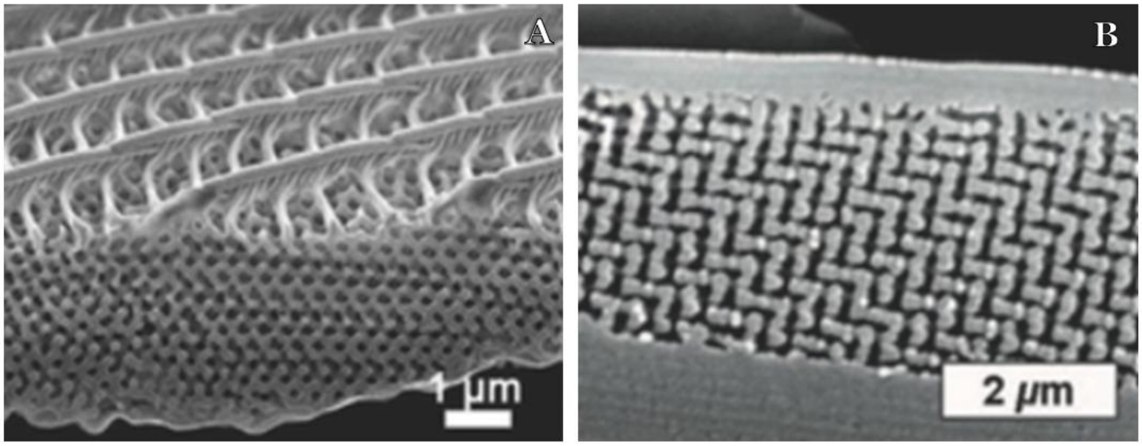

Figure 9: (a) Gyroid Structure in Butterfly Wing and (b) Diamond Structure in Beetle Skeleton [24]

However, due to the self-intersecting design, TPMS are only able to be manufactured using additive manufacturing (AM). Despite this disadvantage, the TPMS were chosen as the optimal candidate for comparison to Honeycomb and use for aerospace applications. As noted in Figure 1, multiple applications cause Honeycomb to be compressed. As such, the compressive strength of the Gyroid, Primitive, and Diamond TPMS will be compared in compression with Honeycomb in both the Axial and Transverse direction.

1.4 Additive Manufacturing Overview

Additive manufacturing (AM) has become a novel manufacturing method in recent years due to numerous advantages. For one, individualized parts that might be needed for repair, customizations, or prototyping can be designed and manufactured much faster using AM than previous manufacturing methods [25]. Furthermore, the printers do not require active attention like many other machines. CNC programmers and tooling are not needed for AM. This means that, other than the pre- and post-processing, workers can spend their time on something else, decreasing labor costs. Finally, AM has the capability to print shapes that cannot be manufactured in any other way, such as TPMS.

Continuous stereolithography (SLA) printing was one of the first AM methods to be patented in 1986 by Charles Hull [26],[27]. This printing process uses ultraviolet light to cure liquid resin that is held in a vat one layer at a time to build a shape from the bottom up [28]. There are two other common types of 3D printing to be considered. First is Fused Deposition Modeling (FDM) that prints by extrusion filament through a heated nozzle. Second is Powder Bed Fusion (PBF) that prints by fusing powder together using an energy source, typically a laser or electron beam [29]. All manufacturing types are shown in Figure 10.

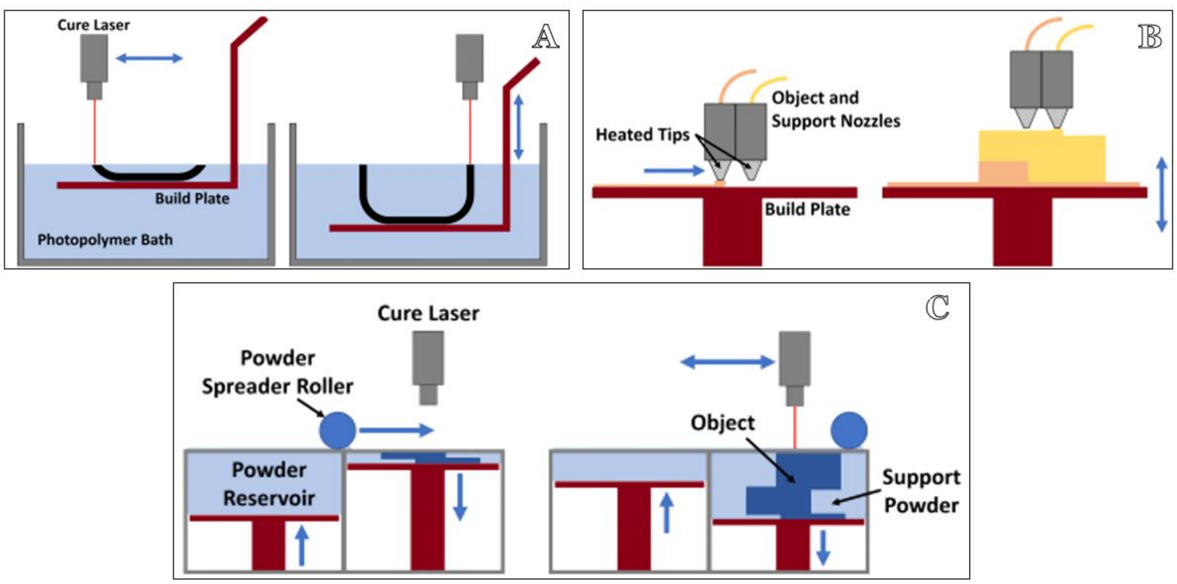

Figure 10: (a) SLA, (B) FDM, and (c) L-PBF Additive Manufacturing Processes [29]

SLA printers have an advantage because they can print at a higher resolution than other types of printers since the resin is cured by light, causing a detailed and smooth finish [28]. However, the process of using a SLA printer can be expensive and time consuming. FDM printers are inexpensive and easy to use but have a disadvantage in anisotropic properties of the final product caused by the wide voids between each layer [30]. PBF can 3D print with metal, but is expensive and can have a rough surface finish due to the energy introduced by the beam [28], [31]. PBF can also be hard to simulate due to the unique properties caused by the fusion of the powder during the manufacturing process [32]. Considering all the advantages and disadvantages of the different types of prints, the SLA printer was chosen for printing the testing samples, because of the high-resolution capability for small prints. Additionally, a L-PBF (Laser Powder Bed Fusion) stainless steel 17-4PH printer was used to print a proof-of-concept sample to ensure that the designs were valid for metal 3D printing. Testing was not done on the metal samples due to the time and cost of manufacturing.

1.5 Previous Work on Compressive Properties of TPMS

The Gyroid structure has previously been tested in compression. One article discussed Gyroid structures that were manufactured using PLA from an FDM printer for compression testing. The Gyroid exhibited ductile failure in compression, and the compression strength increased with an increasing volume fraction [33]. This article proves that for a desired strength, the Gyroid shape can be adjusted accordingly. Furthermore, compression testing was also done on 20MnCr5 SLA Gyroid prints. The samples were reduced by 60% by mass to find mechanical properties. The Young's Modulus was significantly higher on the denser lattice, as suspected [34]. These results show that the Gyroid structure can be used to make a material lighter, while keeping a proportional amount of strength in the structure. Finally, while comparing the strengths of the Gyroid and Primitive lattices in a Finite Element study, the Gyroid was found to have the highest compressive strength [35]. Based on the previous work, the Gyroid should have a higher compressive strength than the Primitive structure.

The Schwarz lattices have also had past research on compressive properties. One article looked at the difference in mechanical properties of the Primitive lattice when adjusting the hole sizes in the structure. The smaller the holes in the Primitive were found, the stronger the structure [36]. This means that the Primitive shape could be adjusted to meet mechanical property needs. There was also research on the Diamond shape using a Ti64 3D printer. This one found that compression strength is related to the porosity of the model [37]. Finally, a similar study was done on the Gyroid, Primitive, and Diamond shapes using PLA to compare the three. The relative density of the lattices was the same. It was found that the Diamond had the highest compressive strength, followed by the Gyroid, then the Primitive [38]. In comparison with the results above, the Gyroid structure should have a higher compressive strength than the Primitive, while the Diamond may have the most effect of all three.

In conclusion, there is already significant research on compressive properties of TPMS shapes using different materials. However, there is no cohesive comparison between all three to Honeycomb for aerospace applications. Further research is needed to find a cohesive result.

1.6 Thesis Outline

This thesis is intended to discuss how TPMS core can be used as an isotropic option in aerospace applications. Chapter 1 discusses the benefit of lattice structures, an overview of Honeycomb sandwich composites, advantages of TPMS, and previous work on the compressive properties of TPMS. Chapter 2 discusses the theory and process of designing the TPMS and Honeycomb, creating and running the simulations, and the chosen lattice size for evaluation. Chapter 3 discusses the SLA additive manufacturing processes used, resolution testing, and manufacturing applications for TPMS. Chapter 4 discusses the compression testing process using the 5969 Series Dual Column Table Frame Instron and the Zeiss Aramis Adjustable Digital Image Correlation System. Chapter 5 discusses compression testing and simulation results of the TPMS and Honeycomb. Finally, Chapter 6 discusses the conclusions of the findings and recommendations for future work.

Chapter 2: Design & Simulation

2.1 Sample Sizing Process

The TPMS samples were sized to ensure that they were comparable to the ordering specifications of Honeycomb manufacturing companies. The following table outlines the possible cell sizes and heights of Honeycomb that can be ordered from various companies. This was used as the basis to decide the cell size and height of the TPMS for testing. Note, that cell size is the size of one repeating shape and height is how tall the sample is compared to its cell size.

Table 1: Honeycomb Size Overview

Company	Cell size (in)	Height (in)
Collin Aerospace	0.125, 0.1875	N/A
Hexcel	0.0625, 0.25, 0.1875	0.5-0.625
ThermHex	0.12, 0.38	0.14-1.1
Easy Composite	0.125, 0.2, 0.25	0.08-0.8
Composite Envisions	0.125	0.125-1
Corex Honeycomb	0.125, 0.25, 0.375, 0.5, 0.75	0.4-1.2
Summary	**0.0625-0.75**	**0.125-1.2**

It must be noted that the companies in Table 1 offer the Honeycomb in a variety of different materials: nomex, aluminum, aramid, and thermoplastics. Aluminum is typically used for aerospace applications, and the thickness of the sheets is a small

0.002 inches. This means that the TPMS would benefit from a comparison with a very thin material. Based on the ordering specifications from the companies listed in Table 1, samples with cell sizes and heights of 0.125-0.5 inches and a thickness of 0.002 inches would be comparable to industry. The resolution of the printer ultimately determined the final sample sizes.

It must be noted that the lattice density for each sample differs. A summary of each lattice density is given in the table below. Sizing based off cell size, height, and thickness caused a difference in density for each space. The strength is normalized by density to account for this difference in the results section. More information about the decision regarding these sample sizes is given in Chapter 3.

Table 2: Lattice Structure Density Comparison

Lattice Structure	**Density (% infill)**
Gyroid	12.22
Primitive	9.22
Diamond	6.56
Honeycomb Axial	7.95
Honeycomb Transverse	7.95

2.2 Theoretical Design of TPMS

All TPMS can be mathematically described using equations in terms of curve *S*. The Gyroid structure can be mathematically described using equations 1 and 2 [21]. The Primitive structure can be mathematically described using equation 3 and 2 [39].

Finally, the Diamond structure can be mathematically described using equation 4 and 2 [39].

$$S_G = \cos(wx)\sin(wx) + \cos(wy)\sin(wz) + \cos(wz)\sin(wx) \tag{1}$$

$$w = \frac{2\pi}{L} \tag{2}$$

$$S_P = \cos(wx) + \cos(wy) + \cos(wz) \tag{3}$$

$$S_D = \sin(wx)\sin(wy)\sin(wz) + \sin(\mathrm{wx})\cos(\mathrm{wy})\cos(\mathrm{wz}) + \cos(\mathrm{wx})\cos(\mathrm{wy})\sin(\mathrm{wz}) \tag{4}$$

The term w is in reciprocal space (in terms of pi) where L is the length of a unit cell. These equations give a way to graph the surface in 3D space using the first term in a Fourier series. The more terms in the Fourier series, the more accurate the mathematical representation of the surface. To reach a perfect surface using mathematics, the terms must go to infinity [39]. However, with current technology, there are easier ways to model the Gyroid, Primitive, and Diamond lattices using Computer Aided Design (CAD) software.

2.2 Parameterized Design of TPMS and Honeycomb

SolidWorks was used to design the TPMS and Honeycomb lattice structures. The design was parameterized so that the dimensions and thickness could be easily changed. Each surface was designed in a similar manner, with different curves. To parameterize a design, an equation was added. This was done by right clicking the "Manage Equations" in the selection tree and adding a name and value for each term. For example, the name could be "unit cell" and the number could be "1/8." Further terms could be added to the list using the previously defined terms as equations. For example, to have a dimension that was always half the unit cell, the equation could be written as “=’unit cell’*0.5”, and that term would automatically calculate the new number when the unit cell number is changed. This process is shown in Figure 11. To input the equations onto the sketch, the “=” on the smart dimension tool was selected and an option appeared to add an equation. This ensured that the whole design could be easily scaled with the change of a couple of numbers.

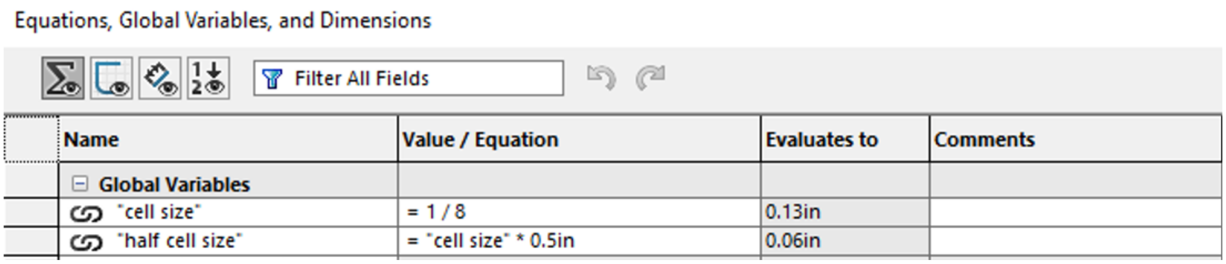

Equations, Global Variables, and Dimensions

Filter All Fields

Name	Value / Equation	Evaluates to	Comments
Global Variables			
"cell size"	= 1 / 8	0.13in	
"half cell size"	= "cell size" * 0.5in	0.06in	

Figure 11: Equation Manager for Parameterized Designs

To start with the TPMS designs, a cube was made with parameterized side lengths, shown in Figure 12. On each face of a cube, lines were drawn. Each line on one face intersects one corresponding line on another face. When finished, this makes one line connected through the faces of the cube. The body of the cube was deleted, and the remaining curves were merged to make a continuous surface. This process is used to make the Gyroid, Primitive, and Diamond structures. The only difference between the structures are the lines on the faces of the initial cube.

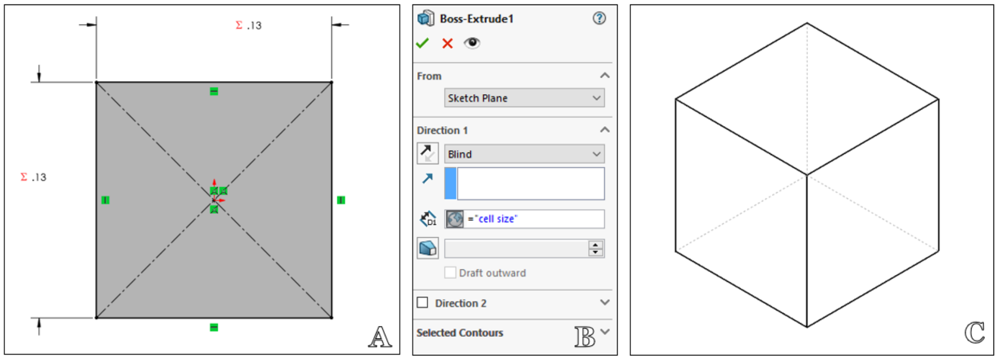

Figure 12: (a) Sketch, (b) Parameterization, and (c) Result of Parametrized Cube

The steps for the design of the Gyroid, Primitive, and Diamond are shown in Figures 13, 14, and 15 respectively. Both the Gyroid and Primitive had a sketch on each side of the parameterized cube. These sketches were merged to make a surface, as mentioned above. The Diamond cell was made in a 3D sketch by tracing the edges of the parameterized cube so that they were constantly connected, and the following curves were merged into a surface. This process was relatively simple to design and parameterize for fast modeling changes. It must be noted that each cube corresponds as an eighth of the cell. The surfaces are moved, rotated, and merged to make the final cell designs. The parametrization of the design allowed for fast changes between cell sizes, heights, and thickness of the lattice structures.

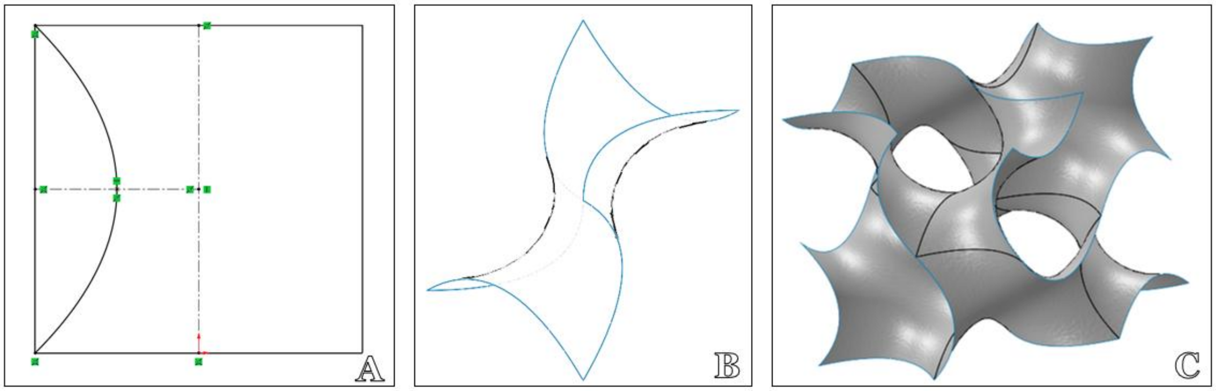

Figure 13: (a) Cube-Face Sketch, (b) Merged Surface, and (c) Final Gyroid Design

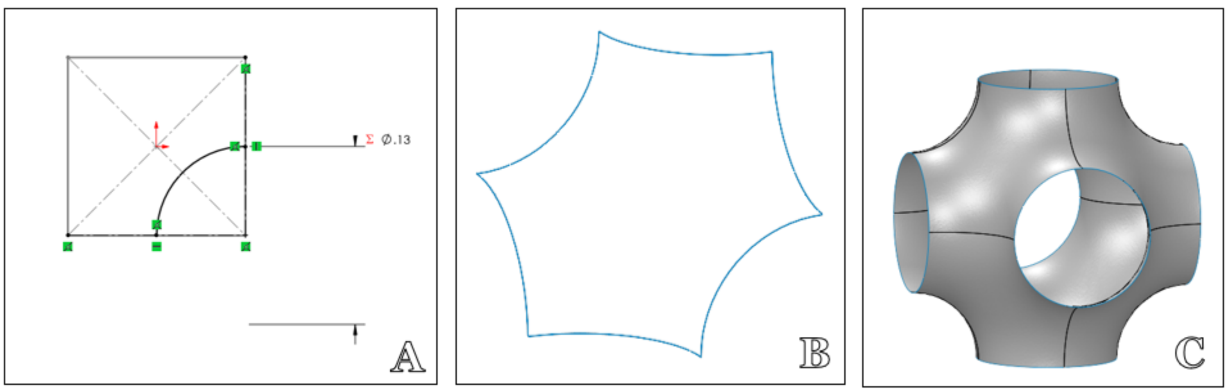

Figure 14: (a) Cube-Face Sketch, (b) Merged Surface, and (c) Final Primitive Design

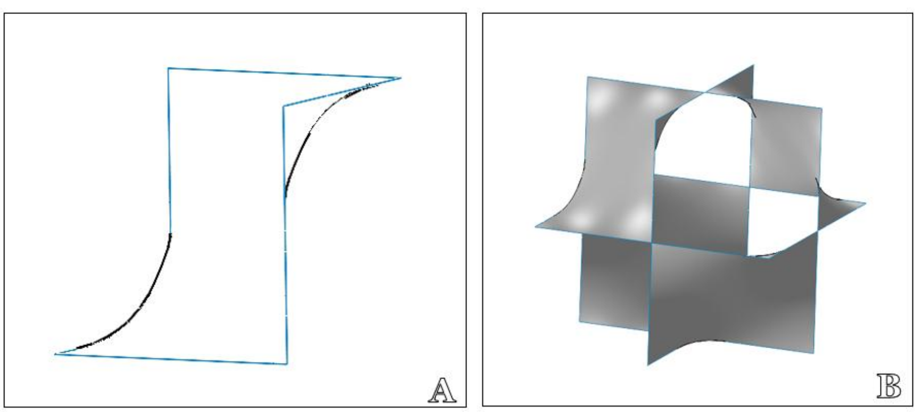

Figure 15: (a) Merged Surface and (b) Final Diamond Design

Designing the Honeycomb structure was simple. SolidWorks has a hexagon shape function. A sketch was drawing using this hexagonal function and extruded to make the Honeycomb surface. The Honeycomb was trimmed in such a way that the hexagonal structure was symmetrical, shown in Figure 16.

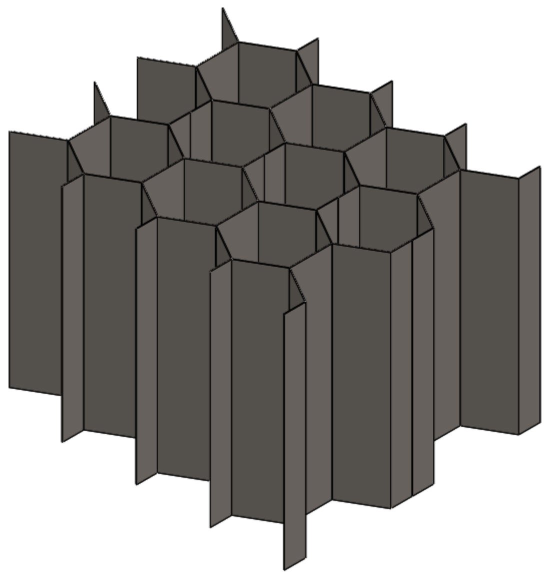

Figure 16: Honeycomb Surface Design

To ensure that the model could be designed for an aerospace application, NACA 0010, NACA 2414, and SC2-0714 Gyroid core airfoils were designed and parameterized. A symmetric, cambered, and super-critical airfoil was chosen to ensure all types of airfoils were designable. These airfoils were modelled, printed, and used as cores for carbon fiber hand lay-ups to ensure the use of TPMS in sandwich composites are manufacturable. The SolidWorks models are shown in Figure 17.

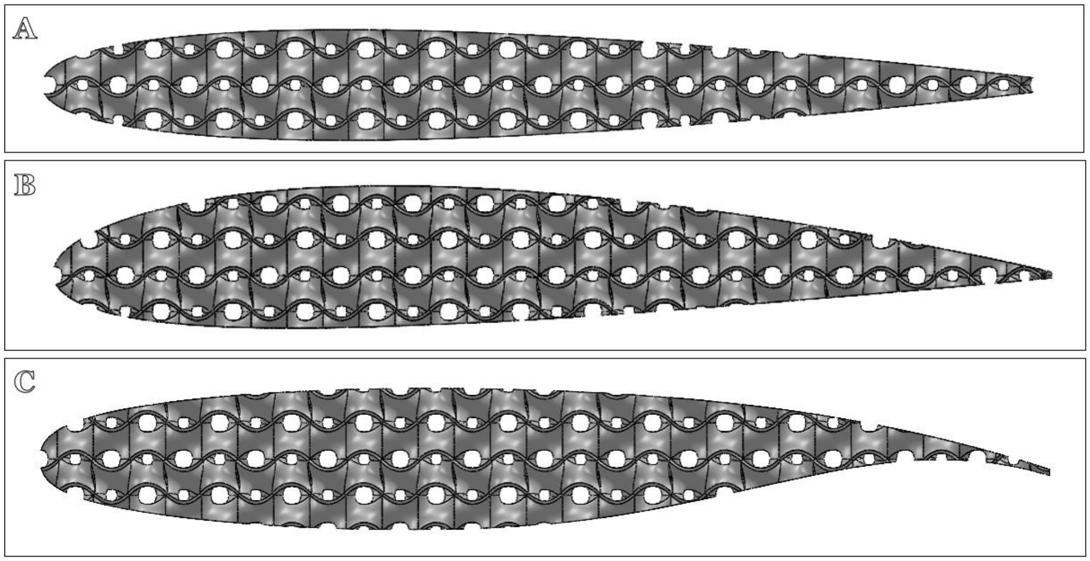

Figure 17: Gyroid Airfoil Designs (a) NACA 0010, (b) NACA 2414, and (c) SC2-0714

2.3 Adjusting the Model for Simulation

The Gyroid, Primitive, and Diamond TPMS were designed to be evaluated for aerospace applications. To start the evaluation, simulations were done to choose the most efficient design. The TPMS models in SolidWorks were converted to simulation software, Ansys. The model was first saved as a .STEP file so it could be accurately uploaded to Ansys Workbench. After Ansys Workbench was opened, there were numerous types of simulations that could be used. Static Structural was chosen by dragging it to the box in the white workspace on the screen. At this point, to import the model, the geometry tab was edited to import the saved .STEP file. To ensure it was uploaded correctly, the model was opened in Ansys SpaceClaim.

After seeing the model was imported correctly, another step was taken to ensure the simulation would run correctly. Using the Workbench tab located at the top, the Share option could be used to ensure that the entire surface will be treated as one structure. Several blue lines appeared on the model indicating that the edges had merged and were treated as one surface. An example of this is shown with the Gyroid in Figure 18.

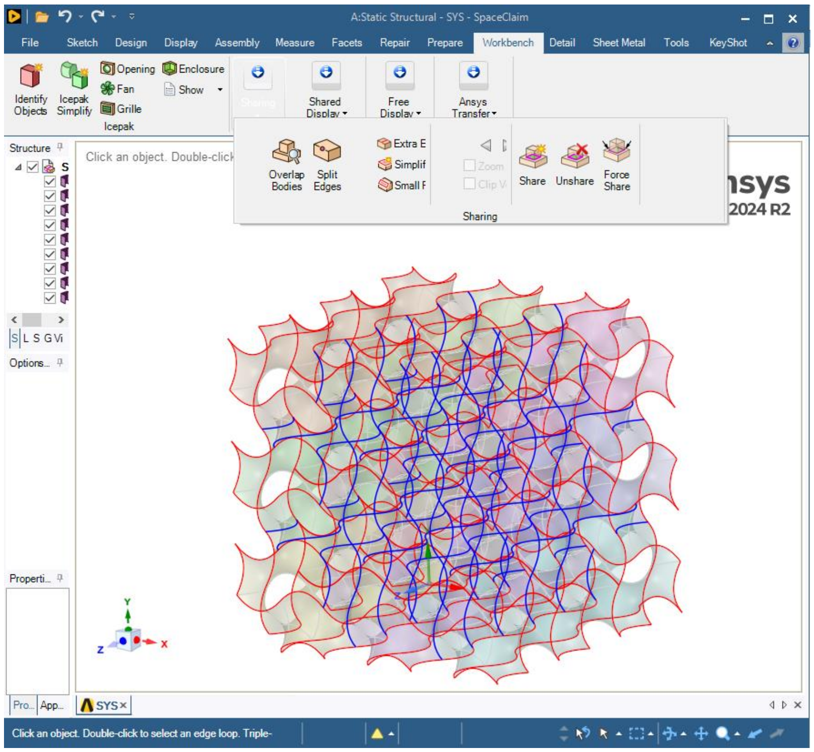

Figure 18: SpaceClaim Share Tool

2.4 Boundary Condition Calculations

The Engineering Data in Ansys Workbench was calculated to be as accurate as possible so that there were reasonable evaluations of the TPMS and Honeycomb prior to testing. The material properties of the resin were given to make a custom material in Ansys that accurately reflects the properties of the standard ANYCUBIC resin. The density, elastic modulus, and Poisson’s ratio are needed to make the custom material, summarized in Table 3.

Table 3: Resin Properties

Resin Density	1.13 $\frac{g}{cm^3}$
Tensile Strength	36-50 MPa
Elongation at Break	7-14%

The tensile strength and elongation at break could be used to calculate the strain and elastic modulus of the material. Due to the isotropic nature of the material, equation 5 was used. Finally, the Poisson's ratio was estimated to be 0.33 based on other polymer resins [40].

$$E = \frac{\sigma}{\varepsilon} = \frac{36}{0.07} = 514\ MPa \qquad (5)$$

To insert the custom material into Ansys Workbench, an Isotropic Elasticity material was added. Next, a custom material was made using the 'Derive from Young's Modulus and Poisons Ratio' option. The resulting material is shown in Figure 19.

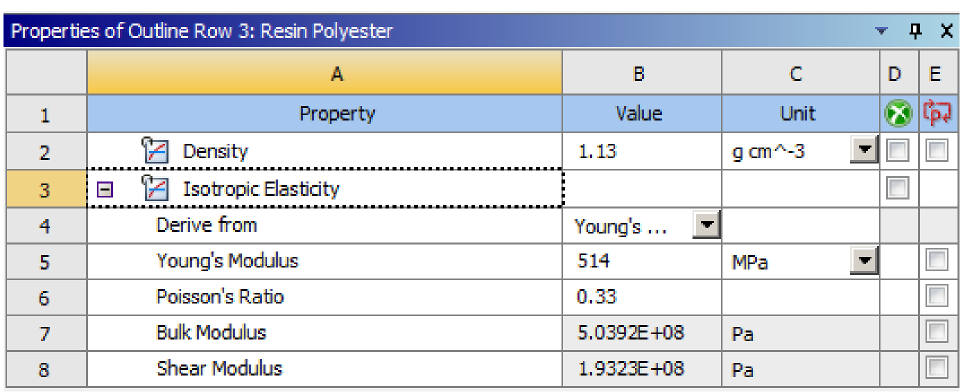
Properties of Outline Row 3: Resin Polyester

	A	B	C	D	E
1	Property	Value	Unit		
2	Density	1.13	g cm^-3		
3	Isotropic Elasticity				
4	Derive from	Young's ...			
5	Young's Modulus	514	MPa		
6	Poisson's Ratio	0.33			
7	Bulk Modulus	5.0392E+08	Pa		
8	Shear Modulus	1.9323E+08	Pa		

Figure 19: Custom Material for Resin

The compression simulation configuration is relatively simple. The edge of the sample that is placed on the machine is modeled as a fixed support, and the top part which is touching the machine is modeled as a force. This should accurately represent what is happening to the sample during the test for the Gyroid, Primitive, and Honeycomb Axial. The Gyroid is given as an example in Figure 20.

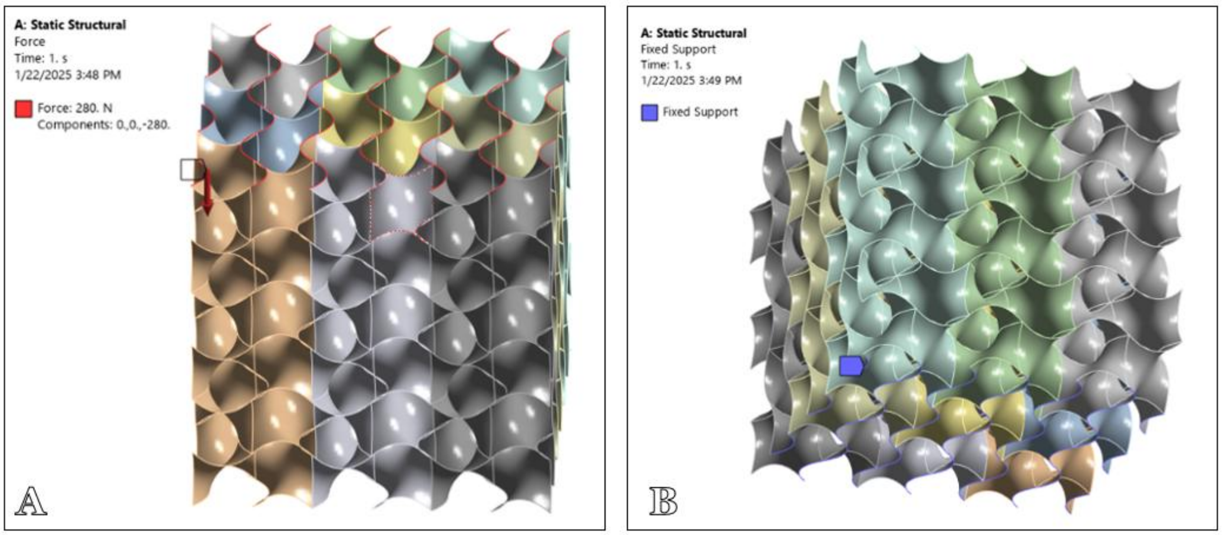

Figure 20: Simulation Boundary Conditions (a) Applied Force and (b) Fixed Support

The Honeycomb Transverse simulation and test configuration were slightly different. The orientation of the Honeycomb was chosen so that the machine would touch an entire cell of the sample. This meant that the Honeycomb Transverse sample needed an additional boundary condition to prohibit movement in the Z direction, because Honeycomb sandwich composite structures typically prevent this movement. A brace was designed for testing to restrict the Honeycomb in the Z direction, and a fixed displacement was used during the Ansys simulation to model the effect, shown in Figure 21.

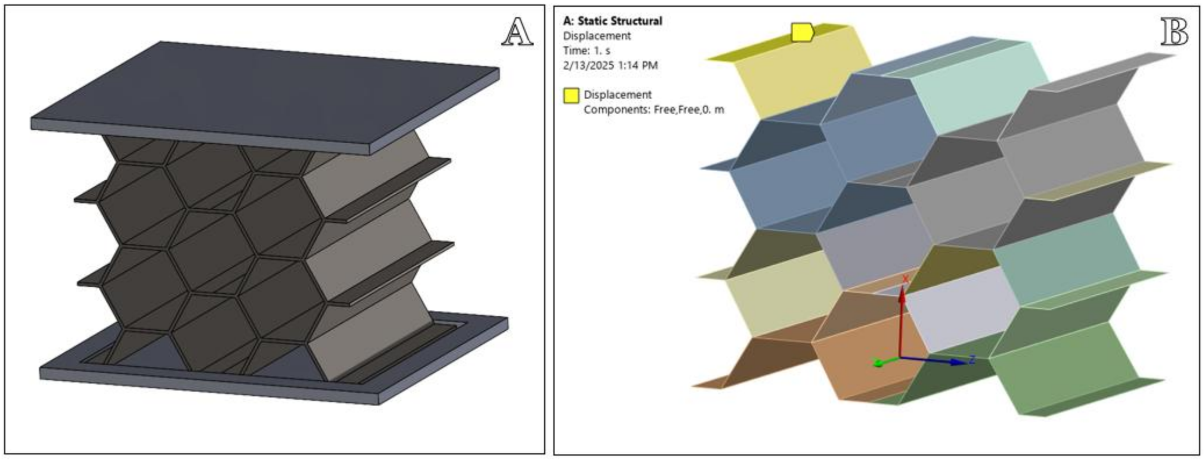

Figure 21: Honeycomb Transverse (a) Testing Configuration and (b) Simulation Configuration

2.5 Optimizing Ansys Mesh

Ansys was used to simulate compression testing on the designs. To ensure the simulations were conservative, the maximum von-Mises stress, maximum principal stress, and maximum shear stress were compared to find the absolute highest stress.

To evaluate three-dimensional structures, Ansys must be evaluated using three-dimensional equations. The stress tensor for a three-dimensional mesh is given in equation 6 and has three normal directions (σ_x, σ_y, σ_z) and six shear directions (τ_{xy}, τ_{xz}, τ_{yx}, τ_{yz}, τ_{zx}, τ_{zy}).

$$\bar{\sigma} = \begin{bmatrix} \sigma_x & \tau_{xy} & \tau_{xz} \\ \tau_{yx} & \sigma_y & \tau_{yz} \\ \tau_{zx} & \tau_{zy} & \sigma_z \end{bmatrix} \quad (6)$$

Von-Mises is a scalar quantity that uses stress applied from any direction in the structure, and in multi-axial loading cases it is typically the highest stress seen [41]. The equation for von-Mises stress is given in equation 7. A visualization of the 3D stress element is shown in Figure 22.

$$\sigma_{vm3D} = \sqrt{\frac{1}{2}[(\sigma_x - \sigma_y)^2 + (\sigma_y - \sigma_z)^2 + (\sigma_z - \sigma_x)^2] + 3((\tau_{xy} + \tau_{yz} + \tau_{zx})^2} \tag{7}$$

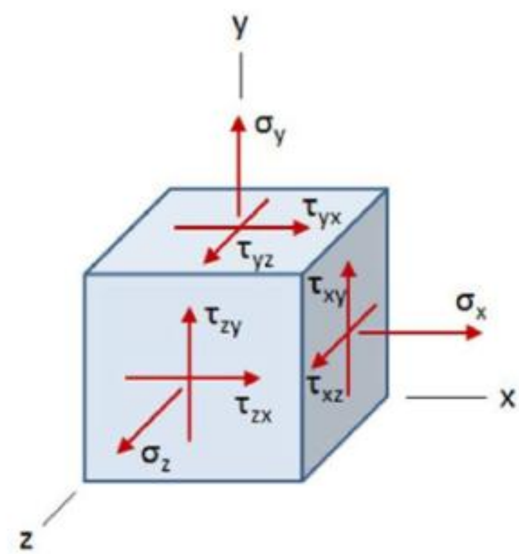

Figure 22: 3D Stress Element [42]

Maximum Principal stress is the stress seen when the coordinate system is arranged so that the shear stress is zero. There are three principal stresses in a three-dimensional system, notated by σ_1, σ_2, and σ_3 ordered from greatest to least. This type of stress defines stress concentration to the normal direction [41]. These are calculated by solving for the eigenvalues in equation 8. Finally, shear stress is the stress seen from loading conditions directed against each other in opposite directions. It is calculated using the principal stresses (equation 9). A mesh is used to obtain these stresses.

$$\det(\bar{\sigma} - \lambda I) = 0 \tag{8}$$

$$\tau_{max3D} = \frac{1}{2}(\sigma_1 - \sigma_3) \tag{9}$$

A mesh consists of a series of nodes and elements that approximate the model into smaller pieces. This allowed the computer to solve different values the users choose, such as stress, strain, and deformation. The size of the mesh could be adjusted to expedite simulation run time. The smaller the mesh, the more accurate the result. However, when running numerous simulations, it was necessary to adjust the model to have a reasonable run time.

One way to expedite the meshing process is to model the structures using surfaces. This allows the computer to split the elements into two-dimensional pieces instead of three-dimensional pieces, which decreases the time for meshing and running the simulation dramatically. As seen in the previous section, the TPMS were designed as parameterized surfaces to account for this. There was a way to add thickness to the model in Ansys Mechanical. Under "Geometry" in the containment tree, the surfaces were selected. An option appeared to insert a thickness. This allowed the model to keep the two-dimensional mesh while considering the thickness of the part. This will reduce the 3D element seen in Figure 22 to a single face, only considering two of the directions. This process simplifies the 3D calculations to the 2D calculations shown in equations 10-12 below.

$$\sigma_{vm2D} = \sqrt{\frac{1}{2}[(\sigma_x - \sigma_y)^2] + 3(\tau_{xy})^2} \tag{10}$$

$$\tau_{max2D} = \frac{1}{2}(\sigma_1 - \sigma_2) \tag{11}$$

$$\sigma_{1,2} = \left(\frac{\sigma_x + \sigma_y}{2}\right) \pm \sqrt{\left(\frac{\sigma_x + \sigma_y}{2}\right)^2 + \tau_{xy}^2} \qquad (12)$$

Another way to expedite the simulation run time was to adjust the mesh size itself. As mentioned above, the smaller the mesh, the better. However, there are limitations to the software. The smallest mesh available to the student version of Ansys is 0.02 inches. However, that is also the mesh that takes the most time to run. A mesh size of 0.04 inches allowed the model to keep its relative shape, while running fast enough to simulate multiple loading conditions within a day.

In conclusion, the Gyroid, Primitive, Diamond, and Honeycomb lattice structures were designed in SolidWorks and parameterized to easily change the cell size, height, and thickness of the samples. Each of the structures were imported into Ansys Workbench for evaluation. The results of the evaluations are discussed in Chapter 5.

Chapter 3: Additive Manufacturing Processes

3.1 SLA Printer Pre-Processing Procedure

The ANYCUBIC D2 SLA printer was used to manufacture samples for testing due to the ease of access through amazon. For the SLA printing process, UV curable resin is a requirement. The ANYCUBIC D2 printer has many options available for purchase: Standard resin, Texture resin, Fast UV-Curing resin, and many more. Due to the abundance of Standard resin available, Standard ANYCUBIC resin was used. To help with the curing of complex geometries, the high clear color was used. Furthermore, the isotropic material had given material properties from the website to assist with evaluation.

The samples were inserted into a software called CHITUBOX for the slicing process. The settings used for the standard resin are summarized in Table 4. The only single-numbered parameters that were changed from the default settings were the bottom layer count (the number of layers considered to be the bottom layers), the exposure time (the amount of time each layer is cured with UV light) and the bottom exposure time (the amount of time the bottom layers are cured with UV light).

Table 4: ANYCUBIC Slicer Settings

Layer Height	0.05 mm
Bottom Layer Count	5
Exposure Time	3.500 s
Bottom Exposure Time	28 s
Transition Layer Count	4
Transition Type	Linear
Transition Layer Interval Time Difference	N/A
Light-off Delay	0.500 s
Bottom Lift Distance	2.000 + 3.900 mm
Lifting Distance	2.000 + 3.100 mm
Bottom Retract Distance	N/A + 0.001 mm
Retract Distance	N/A + 0.001 mm
Bottom Lift Speed	60.000 + 130.000 mm/min
Lifting Speed	30.000 + 120.000 mm/min
Bottom Retract Speed	180.000 + 90.000 mm/min
Retract Speed	180.000 + 100.000 mm/min

There are additional parameters that include a plus sign in their values. Each of the numbers on either side of the plus sign means something different. The only double-numbered parameters that were changed from the default settings were the bottom lift speed, the lifting speed, the bottom retract speed, and the retract speed. Figure 23 has been made to explain what each of these parameters mean.

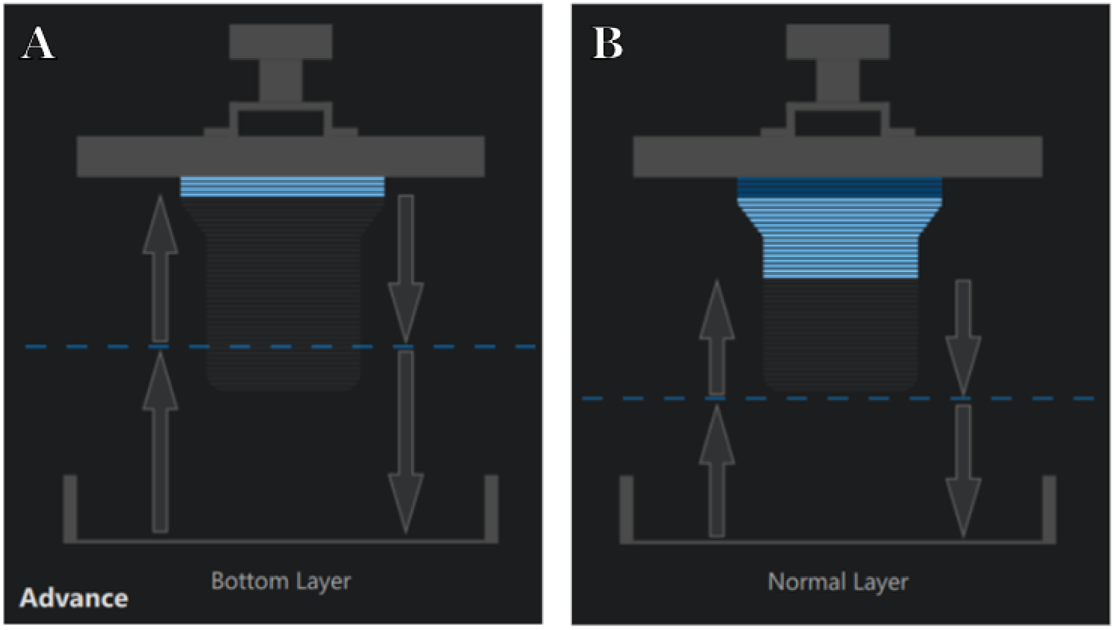

Figure 23: Slicer Settings (a) Bottom Layer (b) Normal Layer

Figure 23a above relates to all the Bottom Layers. This number is specified in the settings. For the Bottom Lift Speed shown in the table above, the 60 relates to the arrow pointing up on the bottom left, and the 130 relates to the arrow pointing up on the top left. For Bottom Retract Speed, the 180 relates to the arrow pointing down on the top right, and the 90 relates to the arrow pointing down on the bottom right. All units are in millimeters per minute.

Figure 23b above relates to all layers not considered the bottom layers, otherwise known as the normal layers, specified in the settings. For the Lifting Speed shown in the table above, the 30 relates to the arrow pointing up on the bottom left, and the 130 relates to the arrow pointing up on the top left. For Retract Speed, the 180 relates to the arrow pointing down on the top right, and the 100 relates to the arrow pointing down on the bottom right. All units are in millimeters per minute.

Each of the lattice structures needed to be evaluated to see if supports were necessary. Due to the SLA printing process, any shape that has a closed loop on the starting surface of the print needs to be rotated to help prevent it from sticking to the resin bed. Due to this, both the Primitive and Honeycomb shape needed to be angled as they were printed, because the Primitive has closed circles as its bottom slice and the Honeycomb has closed hexagons as its bottom slice. The final supports are shown in Figure 24.

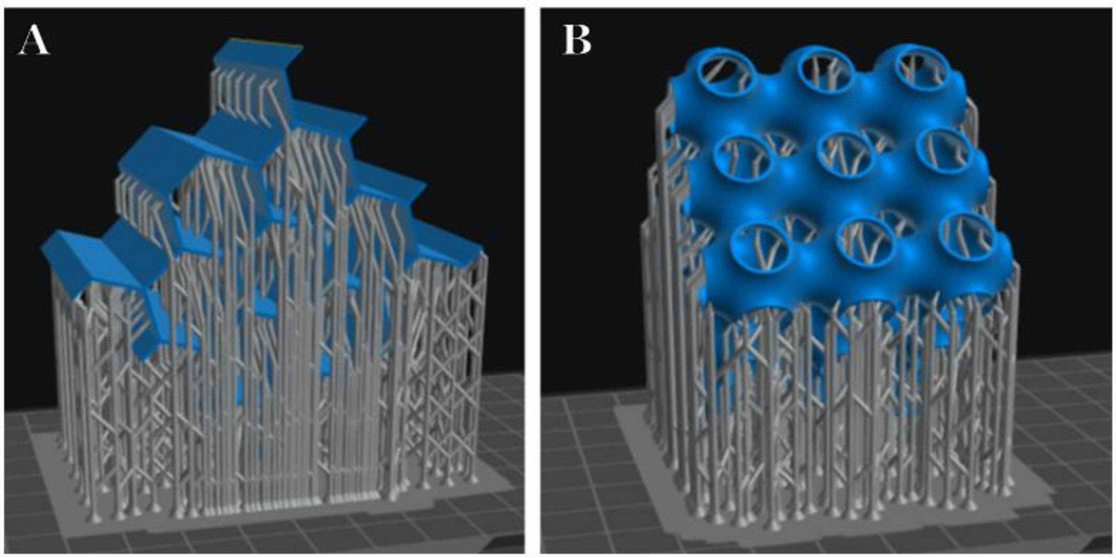

Figure 24: Supports for (a) Honeycomb and (b) Primitive

The Gyroid and Diamond shapes, however, have an open surface as their bottom layer, shown in Figure 25. This meant they were able to be printed without supports. This makes the manufacturing process quick, easy, and highly successful. This was a large reason that the Gyroid was used for resolution testing. The closed surfaces of the initial layers of the Primitive and Honeycomb are also shown in Figure 25. The Gyroid and Diamond have no closed loops, while the Primitive and Honeycomb shapes both have closed shapes that would cause the model to stick to the bottom of the resin reservoir.

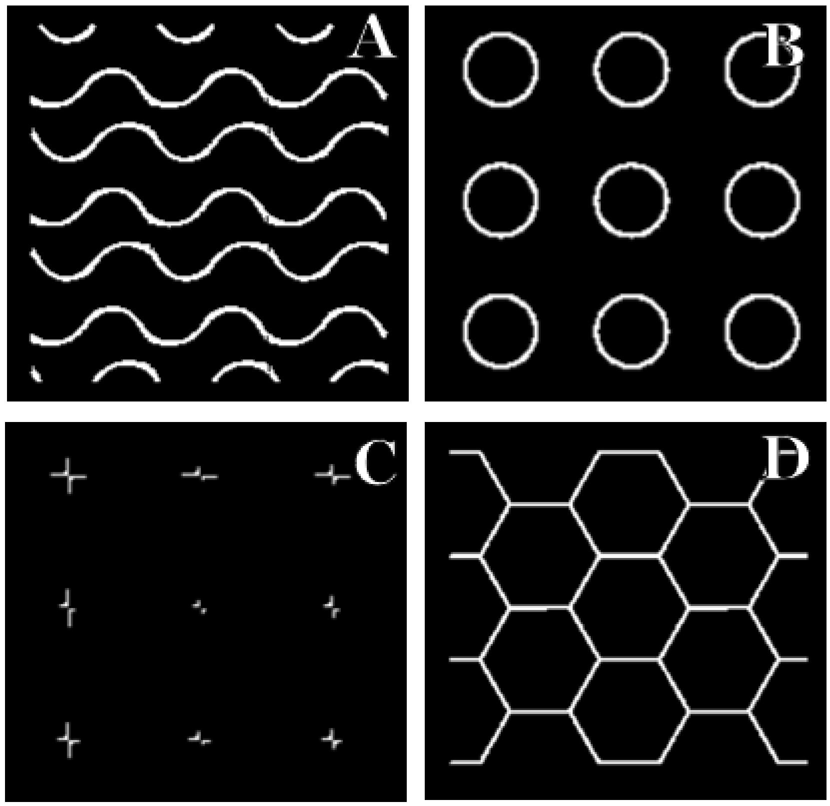

Figure 25: Slice Samples of (a) Gyroid, (b) Primitive, (c) Diamond and (d) Honeycomb

Before the start of each print, the printer was thoroughly cleaned with isopropyl alcohol to ensure that there was no resin between the vat of resin and the glass surface that expels UV light. This ensured that the UV light did not have any problems curing the model to the build plate.

3.2 SLA Printer Post-Processing Procedure

After the prints were finished, there were several steps that were taken to prepare the sample for compression testing. First, the excess resin was removed. This was done by soaking the sample in isopropyl alcohol. This substance absorbs the excess resin that may remain on the sample after it is finished printing. After this, the supports were removed. This was done using a small pair of tweezers to avoid as many defects in the material as possible. Finally, after the sample was fully dried, it was cured in a curing case provided by ANYCUBIC. The manufacturer recommends samples to be cured for 3-5 minutes. The sample was cured for 2 minutes on one side and 2 minutes on the other, following these guidelines. Care was taken not to overcure the samples, as that can degrade mechanical properties.

There were several challenges with the use of an SLA print. First, the issue of the sample sticking to the bottom of the build plate was mentioned in the pre-processing section. This issue was solved by rotating the prints and adding supports. The second problem was file corruption. When using a flash drive, the gcode can corrupt when it is exported. This can cause the print to randomly cure the entire bed, which can be solved by reexporting the file.

3.3 SLA Printer Resolution Testing

The resolution of the ANYCUBIC printer was tested using the information from Table 1 as a basis. It must be noted that the minimum thickness of the ANYCUBIC D2 SLA printer is 0.002 inches, the same as the aluminum sheets mentioned in Section 2.1. As such, the material was tested to see the minimum thickness that the printer was capable of manufacturing. Due to the ease of printing of the Gyroid lattice structures without the need for supports, they were chosen for the resolution comparison.

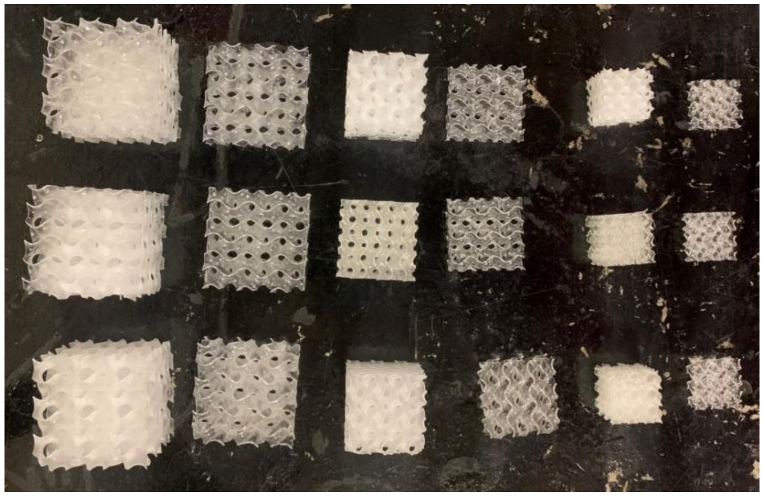

Figure 26: Gyroid Resolution Testing

Figure 26 shows the successful prints from the resolution testing. A total of 18 different cell sizes were successfully printed, with three different cell sizes, three different thicknesses, and two different heights. Thicknesses of 0.004 inches to 0.02 inches were tested, and it was found that 0.01 inches to 0.02 inches thickness was a suitable range. For the cell sizes, one-eighth to one-half inches per cell was tested, and one-fourth to one-half inches was found to be the suitable range. For height, it was found that a height three times the cell size was common in Honeycomb, leading to the 3x3x1 cell size and 3x3x3 cell size test specimen samples. The 3x3x1 unit cell size sample is meant to replicate the Honeycomb typically used in aerospace applications, and the 3x3x3 unit cell size sample is meant to test the abilities of the TPMS replication properties compared to the Honeycomb. The parameterized design made it easy to adjust and test these sizes for printing.

The 3x3x3 cell size samples with the highest thickness were chosen. These were chosen for three reasons. First, the 3x3x3 was chosen for ease of compression testing. There are previous studies of lattices tested in a cube setting, making this size easier to use with the machine. Second, while the 0.01-inch thickness was a suitable range for the Gyroid shapes, it was not suitable for the Primitive and Honeycomb samples, because the removal of the supports would damage the final product. Finally, the 0.5-inch cell size was chosen for ease of use with the Digital Image Correlation System mentioned in Chapter 4. Because of this, the 0.02-inch thickness cube with 0.5-inch cell size samples were chosen for comparison.

The Diamond structure was eliminated as a comparison candidate due to manufacturability and the simulation results. The shape of the diamond is only connected by a small surface between each unit cell. Because of the low thickness in each of the samples, the diamond shape would not be able to be manufactured successfully. The failed print is shown in Figure 27. The simulation results also showed it to be the weakest shape, which is discussed further in Section 5.1.

Figure 27: Diamond Printing Attempt

3.4 Manufacturing for Aerospace Applications

To use the Gyroid shape as core for the small NACA 0010, NACA 2414, and SC2-0714 airfoils shown in Figure 17, multiple steps were taken. First, molds were designed and printed out of PLA for a carbon fiber layup. The molds are shown in Figure 28.

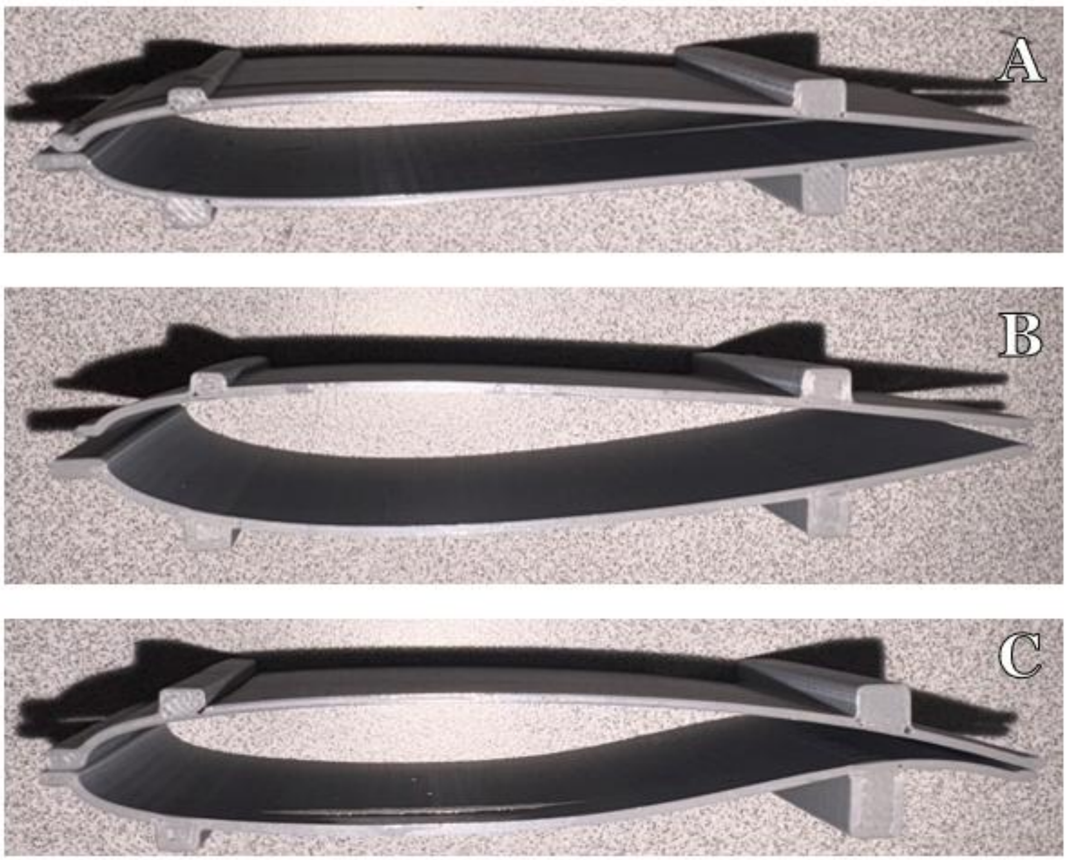

Figure 28: PLA (a) NACA 0010, (b) NACA 2414, and (c) SC2-0714 Airfoil Molds

There are a variety of manufacturing methods to choose from when making a laminated composite, outlined in Section 1.3. A manual wet layup was done, along with compression molding, due to resources available. Figure 29 shows the manual layup process and compression molding processes. Note that epoxy resin is used to bond the filler to the carbon fiber in industry applications, meaning the lattice core can be applied and cured to the fiber as the wet layup is done.

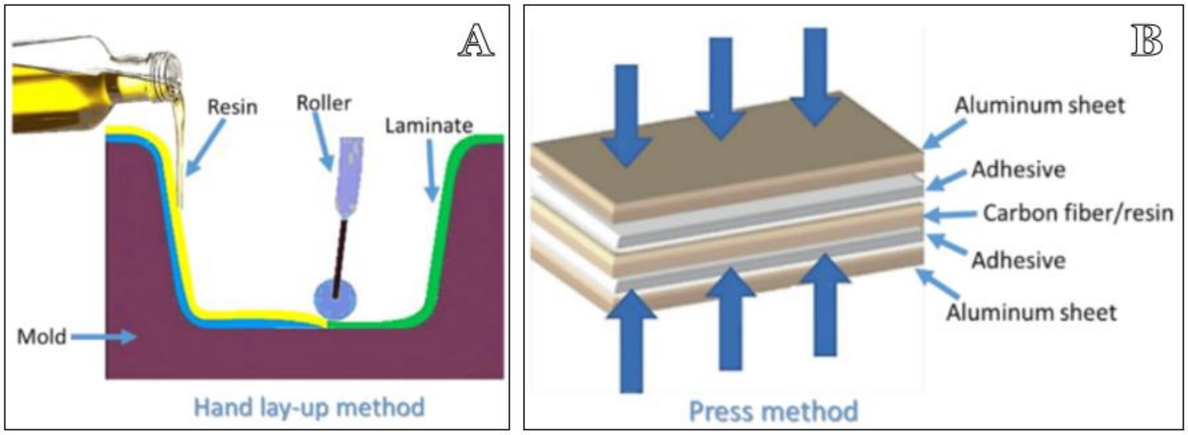

Figure 29: Carbon fiber (a) hand lay-up and (b) press method manufacturing processes [5]

Three proof-of-concept Gyroid core samples were manufactured using the processes shown in Figure 29. First, the peel-apply was used so that the carbon fiber did not bond to the mold when it cured. After this, the carbon fiber was layed-up on the sample with one 0-degree weave and one 45-degree weave. Epoxy was applied between each layer. The Gyroid core was laid on top, and the process was repeated for the top layer. The mold was laid on its side when finished to ensure no extra epoxy was cured within the Gyroid infill. This process is shown in Figure 30.

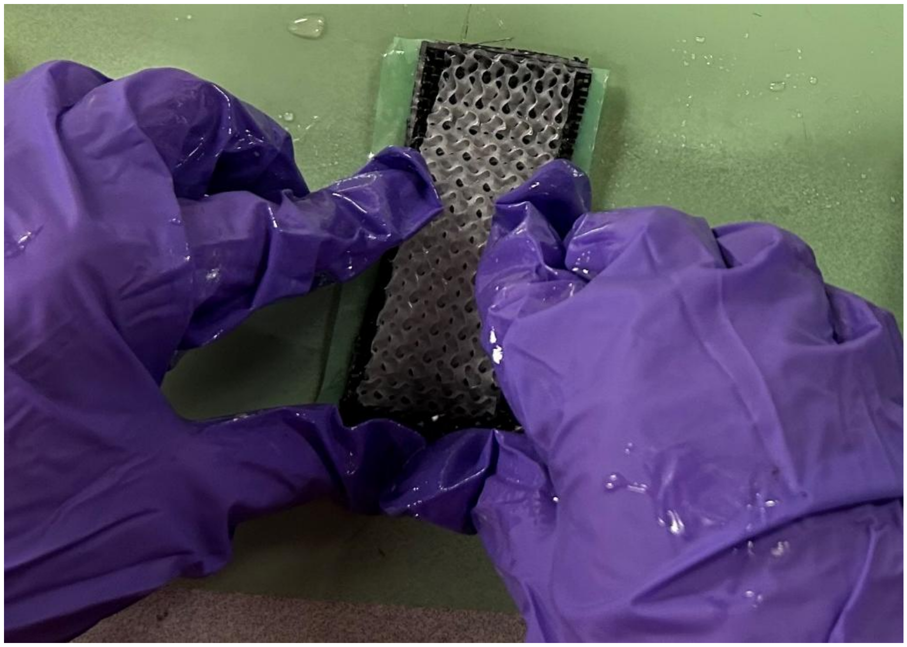

Figure 30: Gyroid Infill Layup Process

Due to the lack of autoclave oven available, the part was lightly compressed and cured for 24 hours at ambient temperature. After this, the mold and peel-apply were removed. The excess of carbon fiber is trimmed to ensure a nice finish. The results are discussed in Section 5.4.

Additionally, it is important to note that there are generally metal lattice structures used in aerospace applications due to their higher strength and durability. To ensure that this structure could be printed using metal, a sample of the Gyroid was printed using stainless steel on the Concept Laser M2 Series 5. The cube lattice thickness was adjusted for easier manufacturing. The thickness was increased to 0.03 inches to a multiple of the thickness of the laser in the L-PBF printer. The results from the metal Gyroid sample are also discussed in Section 5.4.

Chapter 4: Testing Configuration & Procedure

4.1 Compression Test Theory

The 5969 Series Instron and Zeiss Aramis Adjustable Digital Image Correlation System (DIC) were used to measure load, displacement, and localized equivalent strain through the duration of the compression tests. The load and displacement were used to find total stress and total strain. To calculate total strain, the data must first be normalized to ensure that the displacement starts at zero once the Instron starts compressing the material. After this, equation 13 is used to calculate total strain. This equation shows the original specimen length l, and the change in specimen length Δl. The change in length is the normalized displacement measured by the Instron.

$$\varepsilon = \frac{\Delta l}{l} \tag{13}$$

For an isotropic material, the equation for stress is given in equation 14 where P is the applied load and A is the lattice cross-sectional area.

$$\sigma = \frac{P}{A} \tag{14}$$

To find the maximum stress, once again the data must first be normalized to ensure that the measured load starts at zero before the Instron starts compressing the material. The maximum load was used for P in the stress calculations. The lattice cross-sectional area is the cross-sectional area that the lattice occupies in space. In this case, for rectangular lattice samples, the cross-sectional area is simply the total length (l) multiplied by the total width (w) of the lattice sample perpendicular to the application of load P, given in equation 15. A visual representation of lattice cross-sectional area is given in Figure 31.

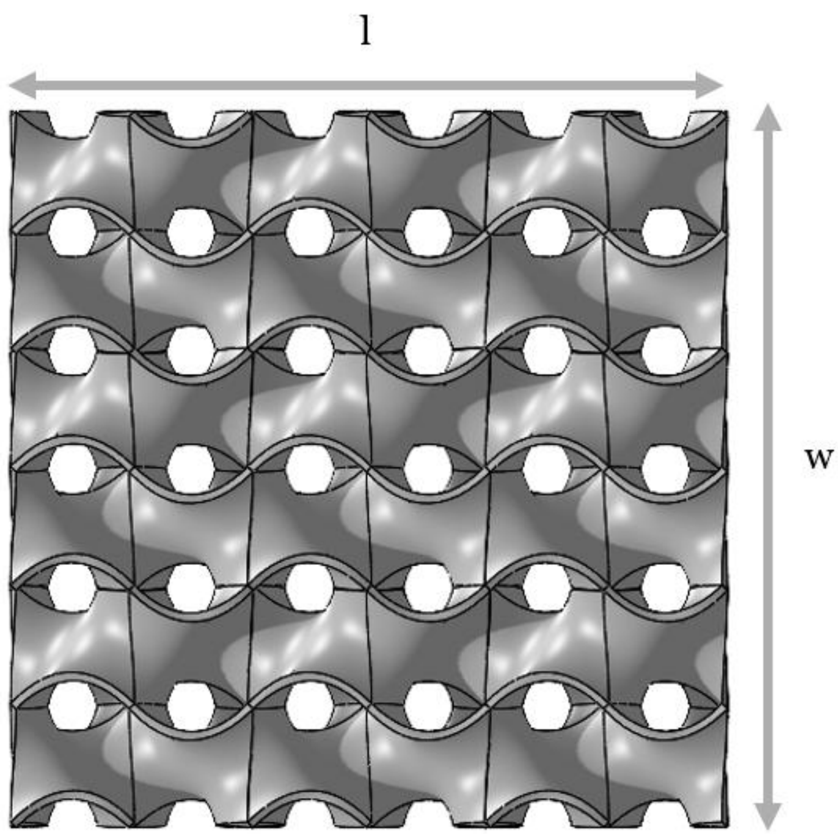

Figure 31: Lattice Cross-Sectional Area

$$A = l * w \tag{15}$$

To calculate the specific strength (*SS*) of each TPMS, the lattice density (ρ) was compared to strength. The lattice density is the mass of the sample divided by the volume of the sample. For a cuboid, the volume (υ) was calculated using the cuboid volume in space that lattice occupies, like the cross-sectional area calculation in Figure 31. The lattice density is shown in equation 16, and the SS calculation is shown in equation 17.

$$\rho = \frac{m}{v} \tag{16}$$

$$SS = \frac{\sigma_{max}}{\rho} \tag{17}$$

4.2 Compression Test Configuration

The 5969 Series Dual Column Table Frame Instron was used to measure load and displacement from the compression tests. The load frame consists of two t-slots parted by a top plate and base beam to hold the slots in place. There is also a moving crosshead to hold the testing adapters. The column has a guide and a ballscrew to move the crosshead up or down. The load string consists of the load cell, grips, adapters, and anything else that is needed between the moving crosshead and the base. There is also a control panel to move the crosshead for testing. A schematic is shown in Figure 32.

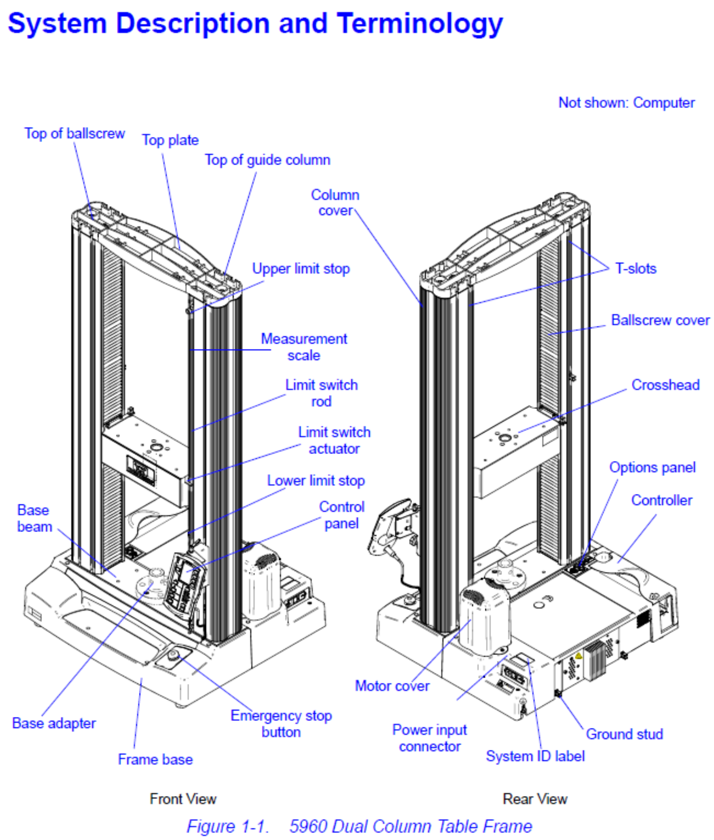

Figure 32: 5960 Series Dual Column Table Frame Instron

A fifty kilonewton load cell was attached to the crosshead. Load cell adapters were fastened both to the bottom plate and the load cell. This allowed the compression plates to be installed for testing. The final test set up is shown in Figure 33.

Figure 33: Compression Test Set-up

The 5969 Instron used the Instron Bluehill software to control the testing systems, collect data, and produce results [19]. To do this, a test method file was made within the software itself. Within this file, the test specimen size, speed of test instrument, and selected exportation of results were some of the key definitions to update. Once a test method was created, it was used multiple times for each test with the same type of specimen.

The Zeiss Aramis Adjustable Digital Image Correlation System (DIC) was used to measure the localized equivalent strain field from the compression tests. The DIC includes a modularly expandable stand for multiple testing configurations, a camera sensor, blue lightening to highlight the contrast of the sample coloring, and Titanar B 75 lenses. A schematic is shown in Figure 34.

Figure 34: DIC Configuration

The samples needed to be prepared for calibration. First, they were spray-painted white. Next, a thin layer of black spray paint was applied to make them appear spotted with an ideal ratio of 60/40 white to black. This ratio allowed the DIC to calibrate the distance between the black dots. This distance would change throughout testing to give an image of the localized strain field. The DIC set-up is included in Figure 33.

The DIC used the 2022 GOM Correlate software. This software connected to the camera to calibrate, evaluate, and determine results. The GOM has a calibration assist to help calibrate the camera by angling the calibration tool at different angles to ensure that the results are as accurate as possible. After the calibration was complete, the measurement was set to a 5M camera size. Next, the camera used the distance between the white and black spots to find the surface of the structure. Sometimes, the number of pixels could be adjusted for the camera to accurately pick up the surfaces of the test specimen. After the surfaces were created, the measuring sequence was specified, and the camera was ready to start recording.

4.3 Compression Test Procedure

The samples were crushed in accordance with ASTM 695-23 Section 9 with a speed of 1.3 millimeters per minute. The samples themselves were sized as a 3x3x3 0.5-inch unit cell size and 0.02 inches of thickness. The process of choosing this sizing was described in Section 3.3

Five samples of each lattice shape were tested for statistical significance. The Gyroid, Primitive, Honeycomb Axial and Honeycomb Transverse samples were crushed using the same speed and placement on the compression plates. The same test method was used for the cube samples in the Bluehill software.

The test specimen was placed on the bottom compression plate. Before the top compression plate was lowered, it was calibrated so that the weight of the plate was not recorded in the results. After this, the top compression plate on the crossbeam was lowered to until just before load was recorded by the Instron. The extension of the plate was zeroed and the Instron and DIC were started at the same time. A note of where the maximum load was taken so a photo of the corresponding strain field could be captured with the DIC.

When the test was finished, the DIC camera was stopped, and the load and extension data were saved to the local computer. These values were able to be easily exported to an excel file for post processing.

Chapter 5: Simulation & Testing Outcomes

5.1 Simulation Results

Simulations were performed on the Gyroid, Primitive, Diamond, and Honeycomb in both the axial and transverse directions. The boundary conditions were calculated using the process outlined in Section 2.4. The simulation was conducted to match the loading conditions present at the compression test. Each model was evaluated until it reached an internal maximum stress of 36 MPa, the resin strength given by the resin manufacturer. The corresponding load was taken as the strength. The von-Mises stress, maximum principal stress, and maximum stress were evaluated until the first of those reached the material stress compacity. The simulations were compared, shown in Figures 35-39.

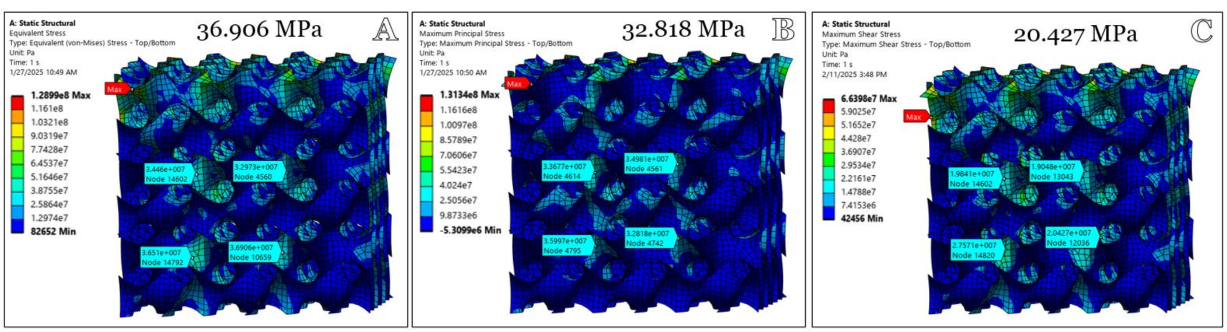

Figure 35: Gyroid (a) von-Mises, (b) Maximum Principal, and (c) Shear Stress

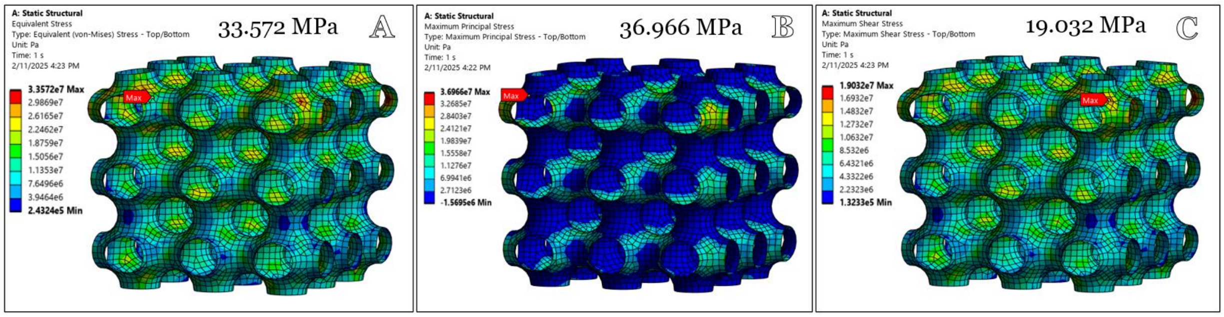

Figure 36: Primitive (a) von-Mises, (b) Maximum Principal, and (c) Shear Stress

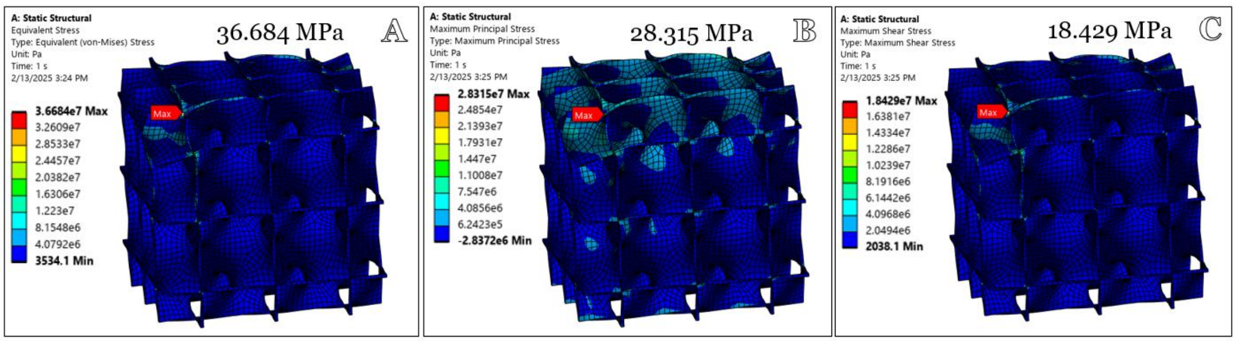

Figure 37: Diamond (a) von-Mises, (b) Maximum Principal, and (c) Shear Stress

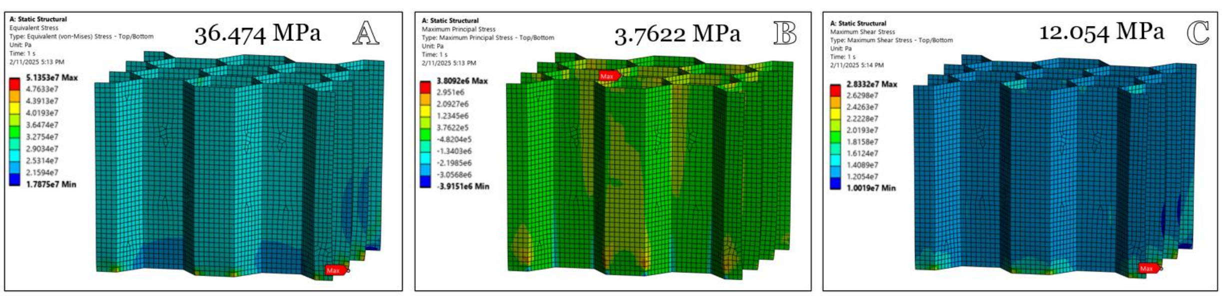

Figure 38: Honeycomb Axial (a) von-Mises, (b) Maximum Principal, and (c) Shear Stress

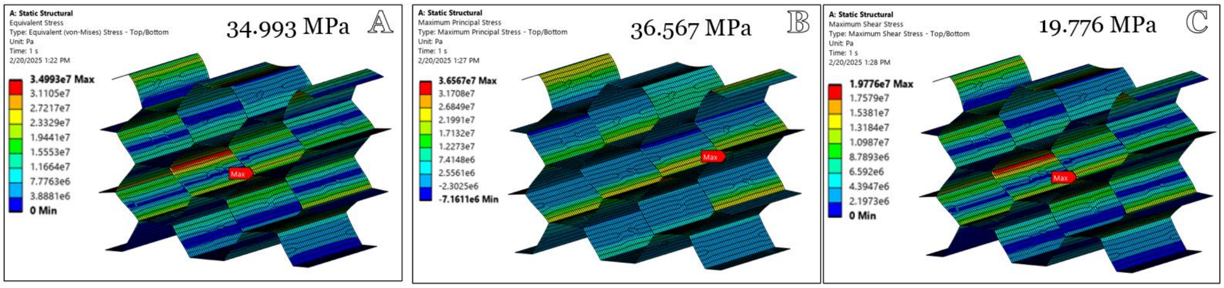

Figure 39: Honeycomb Transverse (a) von-Mises, (b) Maximum Principal, and (c) Shear Stress

After comparing the von-Mises, maximum principal, and maximum shear stresses, the Primitive and Honeycomb Transverse both fail first in maximum principal stress, whereas the Gyroid, Diamond, and Honeycomb Axial and Diamond fail first in equivalent von-Mises stress. As mentioned in Section 2.5, von-Mises is typically the first failure stress. However, since uniaxial loading is applied to the test specimen, failure in the principal directions has a higher chance of being the ultimate failure stress. A comprehensive for compressive strength is shown in Figure 40.

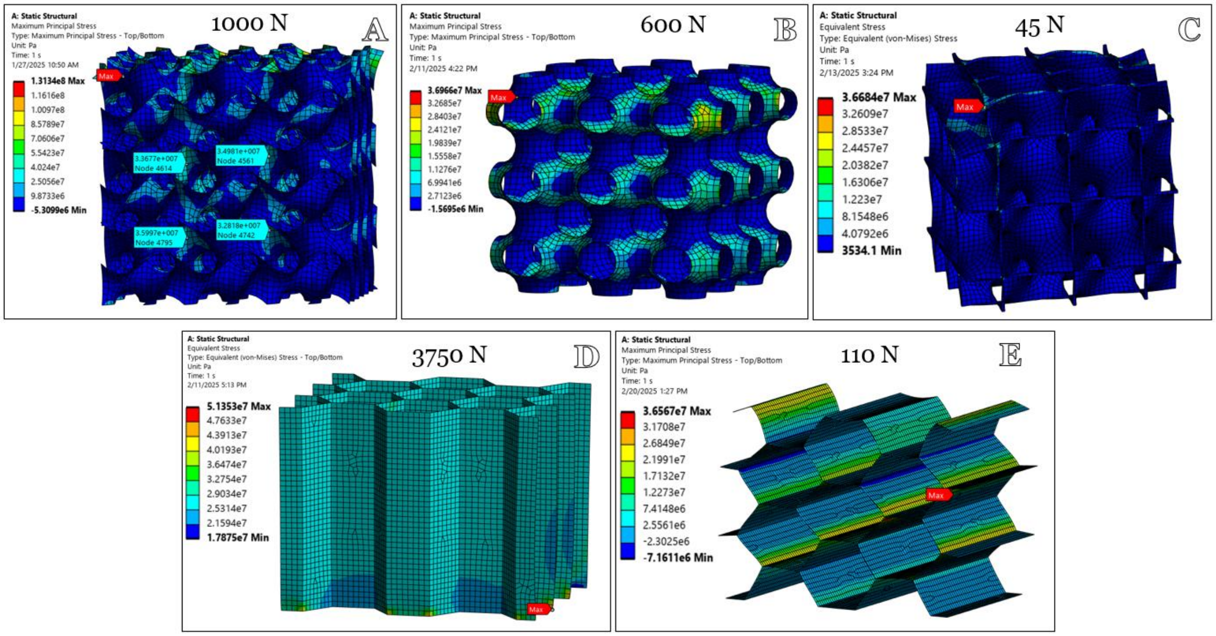

Figure 40: Failure Stress of (a) Gyroid, (b) Primitive, (c) Diamond, (d) Honeycomb Axial, and (e) Honeycomb Transverse

The maximum strength from the simulations, the lattice density, and the strength-to-density ratio are summarized in Table 5. The simulation results indicate the Honeycomb Axial is the strongest per lattice density, followed by the Gyroid, Primitive, Honeycomb Transverse, and Diamond simulations respectively. The results of the simulations indicate that for uniaxial load cases, Honeycomb Axial would be the best choice. However, for load paths in the transverse directions, the Gyroid would be the best option for consideration. The Gyroid strength-to-density ratio is significantly lower than the Honeycomb Axial, but also significantly higher than the Honeycomb Transverse. This means further evaluation of the load cases in all directions would need to be explored to decide if the Gyroid core is the best option for sandwich composites. Furthermore, the Diamond structure is extremely weak with the 0.002-inch thick walls.

The simulation results indicate that the Diamond should be removed as a candidate for testing.

Table 5: Lattice Simulation Comparison

Lattice	Strength (N)	Lattice Density ($\frac{kg}{m^3}$)	Strength-to-Density Ratio ($\frac{N}{\frac{kg}{m^3}}$)
Primitive	600	107.015	5.607
Gyroid	1000	137.926	7.250
Diamond	45	87.740	0.513
Honeycomb Axial	3750	115.651	32.425
Honeycomb Transverse	110	116.883	0.941

5.2 Compression Testing Results

The Gyroid, Primitive, and Honeycomb compression testing results were evaluated for aerospace applications. The normalized maximum strength calculated from the Instron during testing, the lattice density, and the strength-to-density ratio are summarized in Table 6. These results indicated the same conclusion made from the simulations, that for uniaxial load cases, Honeycomb Axial would be the best choice, and for transverse load paths, the Gyroid could be a better option. Furthermore, as seen in the simulations, the Gyroid strength-to-density ratio is significantly smaller than the Honeycomb Axial, and significantly higher than the Honeycomb Transverse.

Table 6: Lattice Strength-to-Density Comparison

Lattice	Lattice Strength (N)	Lattice Density ($\frac{kg}{m^3}$)	Strength-to-Density Ratio ($\frac{N}{\frac{kg}{m^3}}$)
Gyroid	785.025	137.926	5.692
Primitive	554.566	107.015	5.182
Honeycomb Axial	3023.588	115.651	26.144
Honeycomb Transverse	117.815	116.883	1.008

It must be noted that specific strength is slightly different than the ratios mentioned above. Specific strength uses strength in terms of Pascals instead of Newtons. The specific strength was not used in the simulation section because each sample was evaluated to 36 MPa, making the specific strength calculation meaningless in this instance.

To ensure the calculations using the Instron data are valid, the specific strength was calculated and compared to similar tests. The lattice density and specific strength are calculated using the process outlined in Section 4.1 and equations 16 and 17. These results are shown in Table 7. A similar test used an SLA printer to compare three lattice structures: Fluorite, FCC, and BCC structures. The results indicated the specific strength to be between 6.0E+03 and 2.2E+04 $\frac{Nm}{kg}$ [43]. The results in Table 7 are comparable to the results seen in the previous study, validating the lattice density calculation indicated in Section 4.1.

Table 7: Lattice Specific Strength Comparison

Lattice	**Lattice Strength (Pa)**	**Lattice Density ($\frac{kg}{m^3}$)**	**Specific Strength ($\frac{Nm}{kg}$)**
Gyroid	5.41E+05	137.926	3.92E+03
Primitive	3.82E+05	107.015	3.57E+03
Honeycomb Axial	2.08E+06	115.651	1.80E+04
Honeycomb Transverse	7.04E+04	116.883	5.99E+02

The load versus extension was graphed from the data given by Instron. Figures 41 and 42 show that the Honeycomb Axial was clearly the strongest choice, with the Honeycomb Transverse being the weakest. Notice the Honeycomb Transverse had a single point of failure, which could be seen when the load drops. In the 7.263g sample, the load reached a higher point after the first crack, shown by the increasing graph after a short drop. The other samples had complete failure after the initial failure of the material, which is why the graph ends after reaching its highest point.

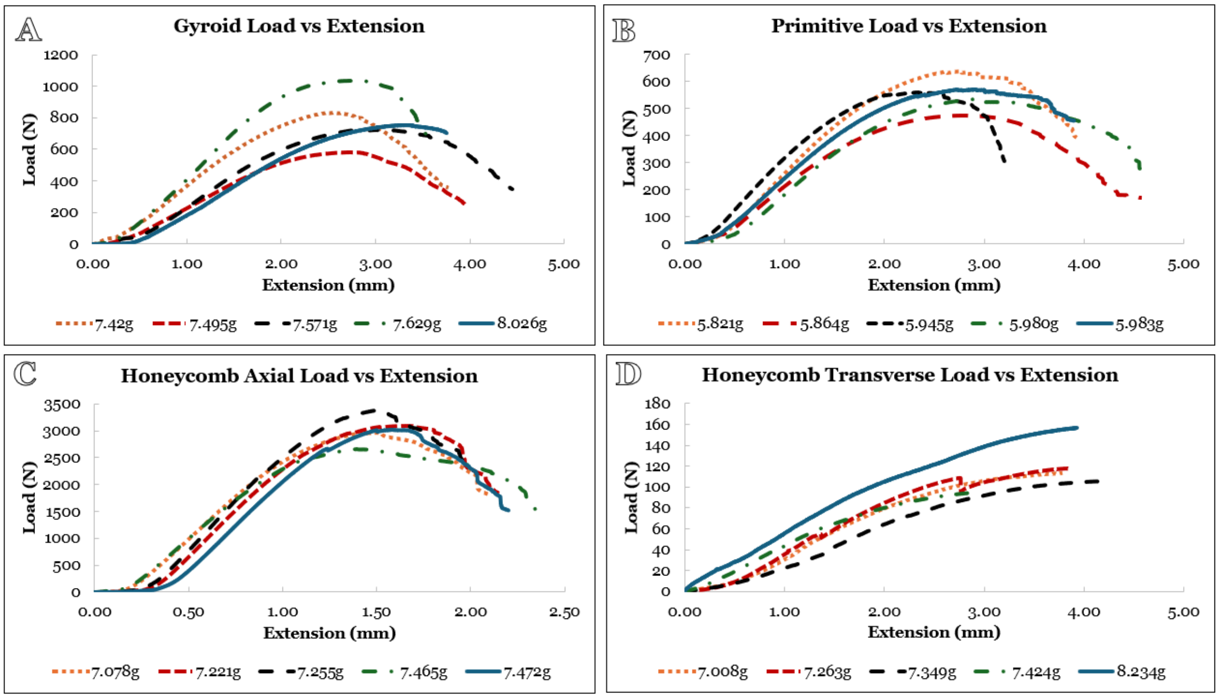

Figure 41: Load vs Extension of (a) Gyroid, (b) Primitive, (c) Honeycomb Axial, and (d) Honeycomb Transverse

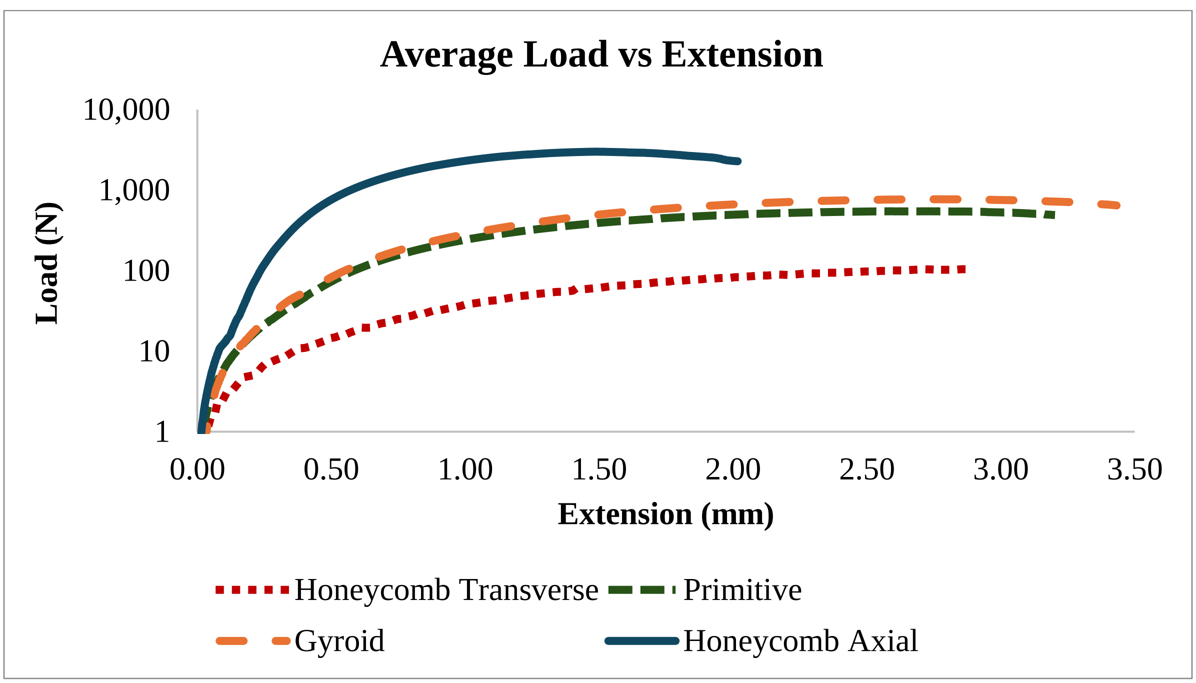

Figure 42: Average Load vs Extension

Finally, the total stress and total strain values were calculated and plotted for comparison. The process used to calculate stress and strain was given in Section 4.1. These results are used to understand the consistency of the tests, as well as give a visual comparison of the different Elastic Modulus's of the structures. Results are shown in Figure 43.

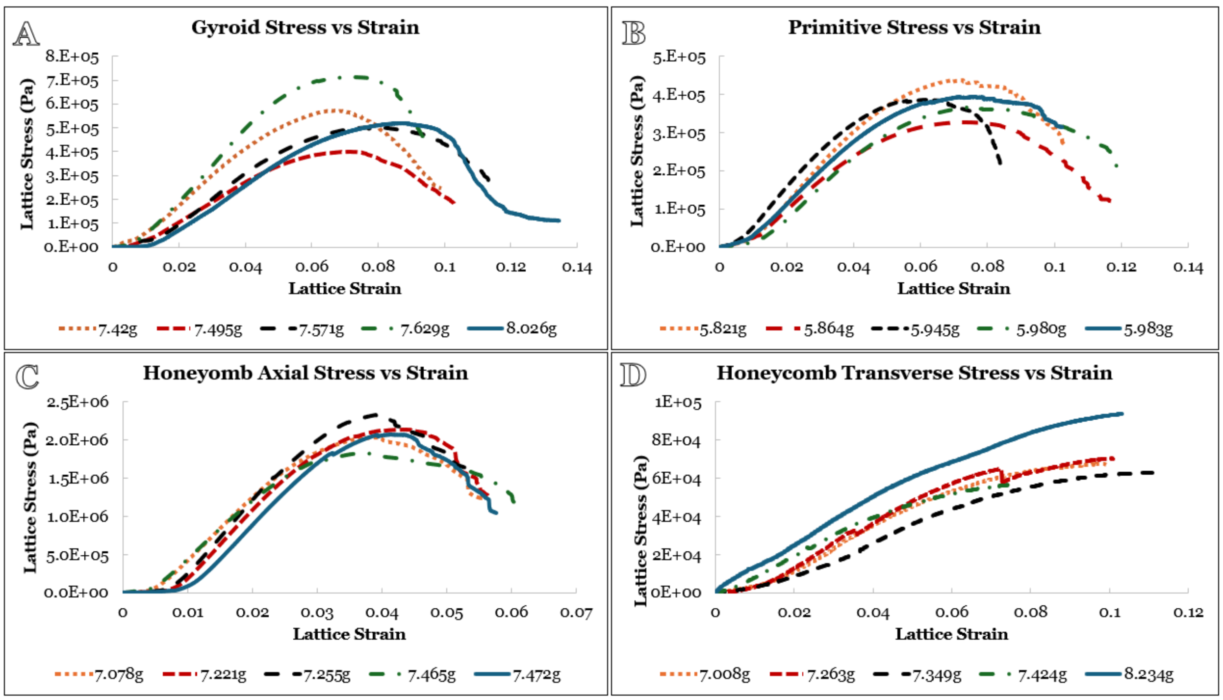

Figure 43: Stress Strain Curve of (a) Gyroid, (b) Primitive, (c) Honeycomb Axial, and (d) Honeycomb Transverse

First, consistency of the results can be seen in both Figure 41 and 43. The results of the Honeycomb Axial were the most consistent in both the Load vs Displacement graphs and the Stress-Strain curves. Following were the Primitive and Honeycomb Transverse. The Gyroid had the least consistent results. These results, specifically with the Gyroid, are not consistent with the order of strength-to-density ratios seen in Table 6. This might be the case because during post processing the samples were rinsed with isopropyl alcohol then set to dry before curing in the curing oven. Due to the geometry of the Gyroid, it was harder to tell when it was dry. There may have been some isopropyl alcohol left in the sample when they cured that could account for the lack of consistency. Despite this, the results were consistent enough to be used in the average calculations.

Looking specifically at Figure 44, the relative Elastic Modulus of the shapes can be compared. The Honeycomb Axial has the highest elastic modulus, seen by the slope of the stress-strain curve. Following that is the Gyroid, then Primitive, then Honeycomb Transverse. These results are as expected based on the strength-to-density calculations in Table 6. Furthermore, the Gyroid and Primitive both have similar Elastic modules, with the Gyroid being slightly higher. This means that when loaded in the transverse direction, either option would be better than the Honeycomb. Finally, as expected from the strength results, a higher load corresponds with a higher stress for the same cross-sectional area.

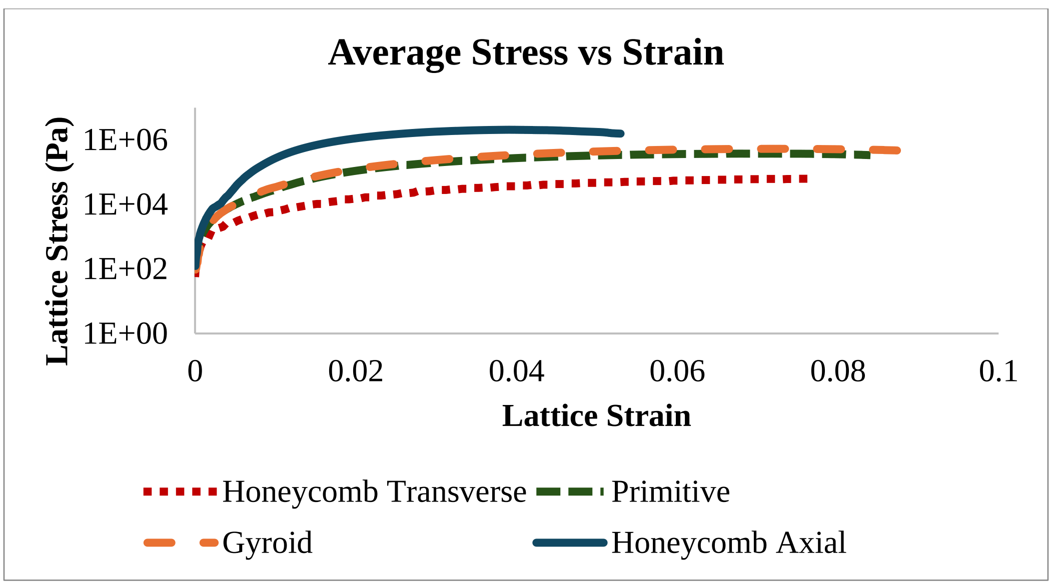

Figure 44: Average Stress-Strain Curves

5.3 Testing Comparisons

The simulation results were compared to the testing results to validate the simulation methods. If the results were the same, that meant simulation could be used to evaluate further shapes without the need to test every sample. This would save time and materials from printing and testing. The results from the simulation and the compression tests are compared in Table 8. These results show that the simulation results were very similar to the testing results and followed the same trend. This means the method of simulations used in this report are a valid way to evaluate future designs to save cost on materials and time in testing.

Table 8: Simulation vs Testing Results

Lattice	**Simulation Ratio ($\frac{N}{\frac{kg}{m^3}}$)**	**Testing Ratio ($\frac{N}{\frac{kg}{m^3}}$)**
Primitive	5.607	5.182
Gyroid	7.250	5.692
Honeycomb Axial	32.425	25.144
Honeycomb Transverse	0.941	1.008

Next, the results from the DIC strain field were compared to the simulations. The same simulation used to find the strength was used to find the strain field. The von-Mises strain can be found directly from Ansys. Results from the simulations are compared to the DIC results in the following figures. The scales of the DIC results were adjusted to match the scale from the simulation to make a direct comparison to the results. The photos using the DIC were taken at the time of the maximum load. Note that localized equivalent strain is shown for both the simulations and the DIC.

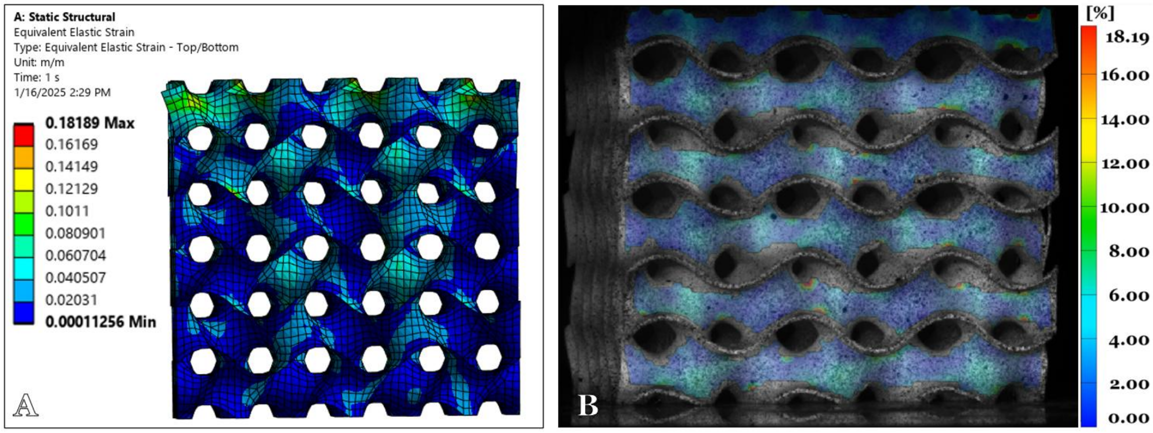

Figure 45: Gyroid Equivalent Strain Field (a) Simulation and (b) DIC

Figure 45 shows that the strain field is 18.19% for the Gyroid. This strain is significantly higher than the strain rate of the resin (7%-14%), meaning the Gyroid shape has the ability to increase localized strain before failure. The general areas of high strain, near the middle of the sample, are the same in both the simulation and the tests. The scale from the test has been normalized to make an accurate comparison.

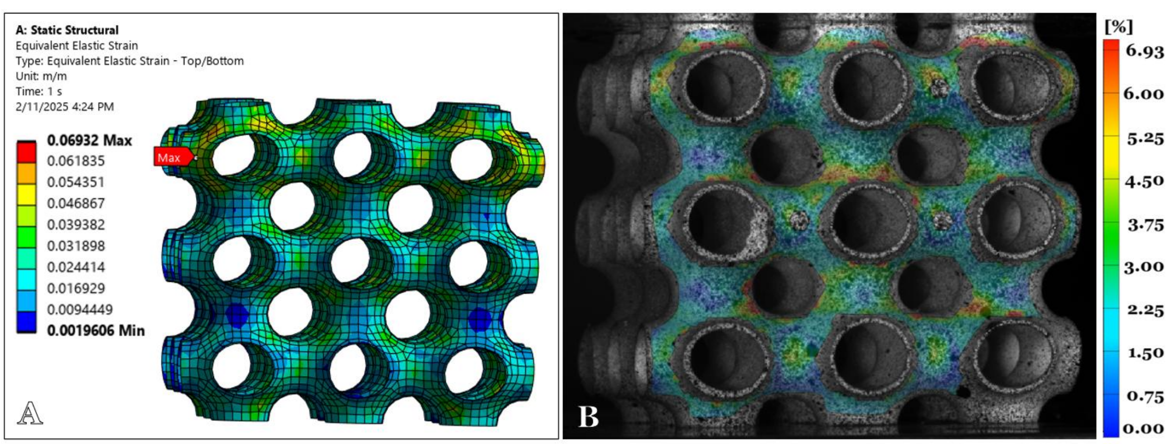

Figure 46: Primitive Equivalent Strain Field (a) Simulation and (b) DIC

Figure 46 shows that the strain field is close to 6.93% for the Primitive. This strain is comparable to the strain given by the resin manufacturer (7%-14%). The highest strain areas correlate to the high stress areas from the simulation. The higher strain spreads outwards perpendicularly from the applied load in both the simulation and the test.

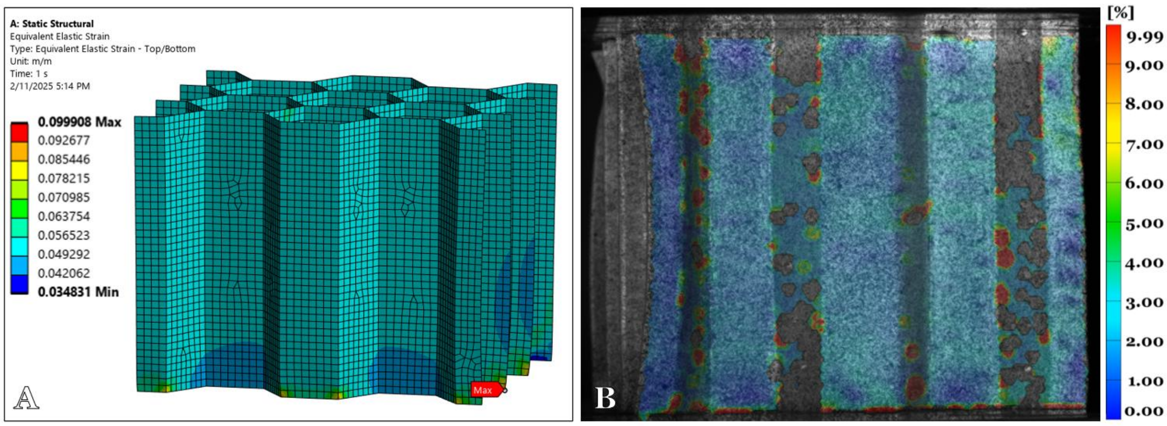

Figure 47: Honeycomb Axial Equivalent Strain Field (a) Simulation and (b) DIC

Figure 47 shows that the strain field is 9.99% for the Honeycomb Axial. This strain matches the strain given by the resin manufacturer (7%-14%). The strain is uniform throughout the structure. The highest strain throughout the part occurs at the location of the applied load. This can be seen in the results from the test, and Honeycomb fails extremely fast in the axial direction.

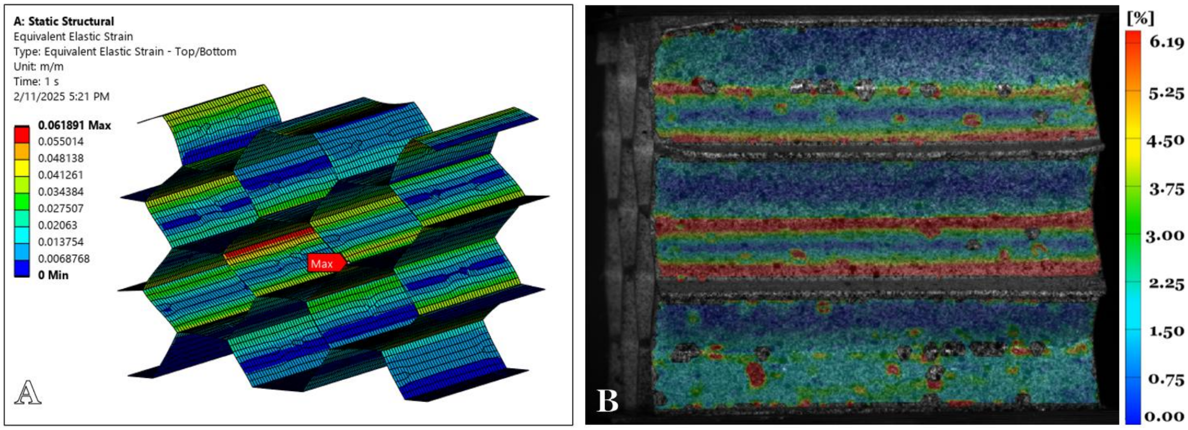

Figure 48: Honeycomb Transverse Equivalent Strain Field (a) Simulation and (b) DIC

Figure 48 shows that the strain field is 6.19% for the Honeycomb Transverse. This strain is comparable to the strain given by the resin manufacturer (7%-14%). The strain is at the highest along the joints of the hexagon structure. This can be seen in both the simulation and the DIC. This is also the location of failure during both the test and the simulations.

In conclusion, the Gyroid can withstand higher localized deformation compared to the other structures. The Primitive, Honeycomb Axial, and Honeycomb Transverse deform in accordance with 7-14% elongation at break, the material properties given by the resin manufacture given in Table 3, while the Gyroid can withstand up to 18% elongation before break. This means if something needed to be designed to withstand a high localized strain, the Gyroid would be the best option. Overall, the simulations once again match the testing. The locations of higher and lower localized strains match that of the simulations. This is another validation that simulations can be used to evaluate potential designs.

5.4 Aerospace Applications

To prove that Gyroid core is valid to use in sandwich composites, an airfoil was designed, printed, and manufactured. The design is discussed in Section 2.2, and the manufacturing process is described in Section 3.4. As a reminder, the Gyroid shape differs from the Honeycomb due to the open geometry on all sides. This can be seen by a sample of the slices in Figure 25a. To ensure that the epoxy would bond to an open structure, the layup was done with minimal pressure. The Gyroid successfully bonded to the carbon fiber during manufacturing, meaning it would be a valid core for sandwich composite application. The results of the sample are shown in Figure 49.

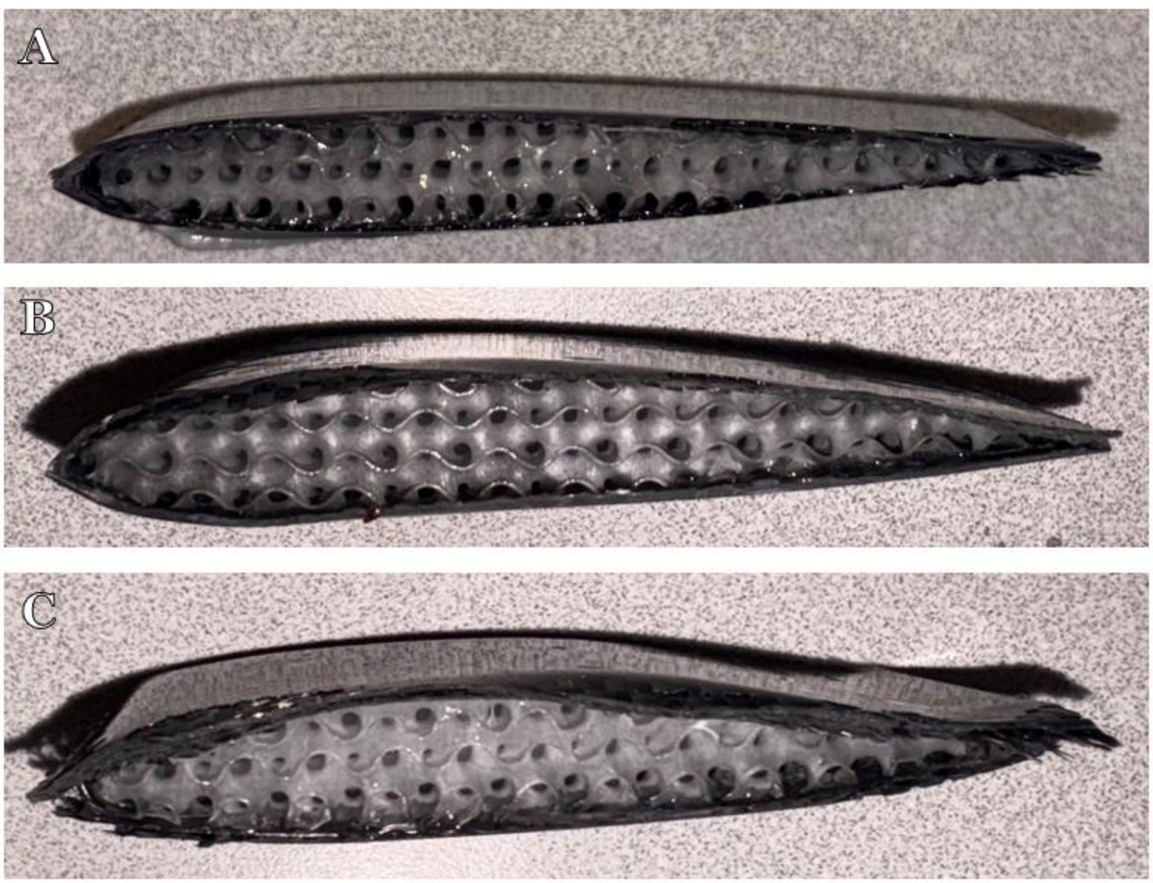

Figure 49: Carbon Fiber Gyroid Infill (a) NACA 0010, (b) NACA 2414, and (c) SC2-0714 Airfoil Samples

Additionally, a single sample was printed on an L-PBF stainless steel printer to ensure this design could be printed out of metal. The Concept Laser M2 Series 5 was used for a proof-of-concept print. Testing was not done on these samples due to the cost of printing and time constraints. Overall, the print was very successful. The final stainless-steel sample is shown in Figure 49a.

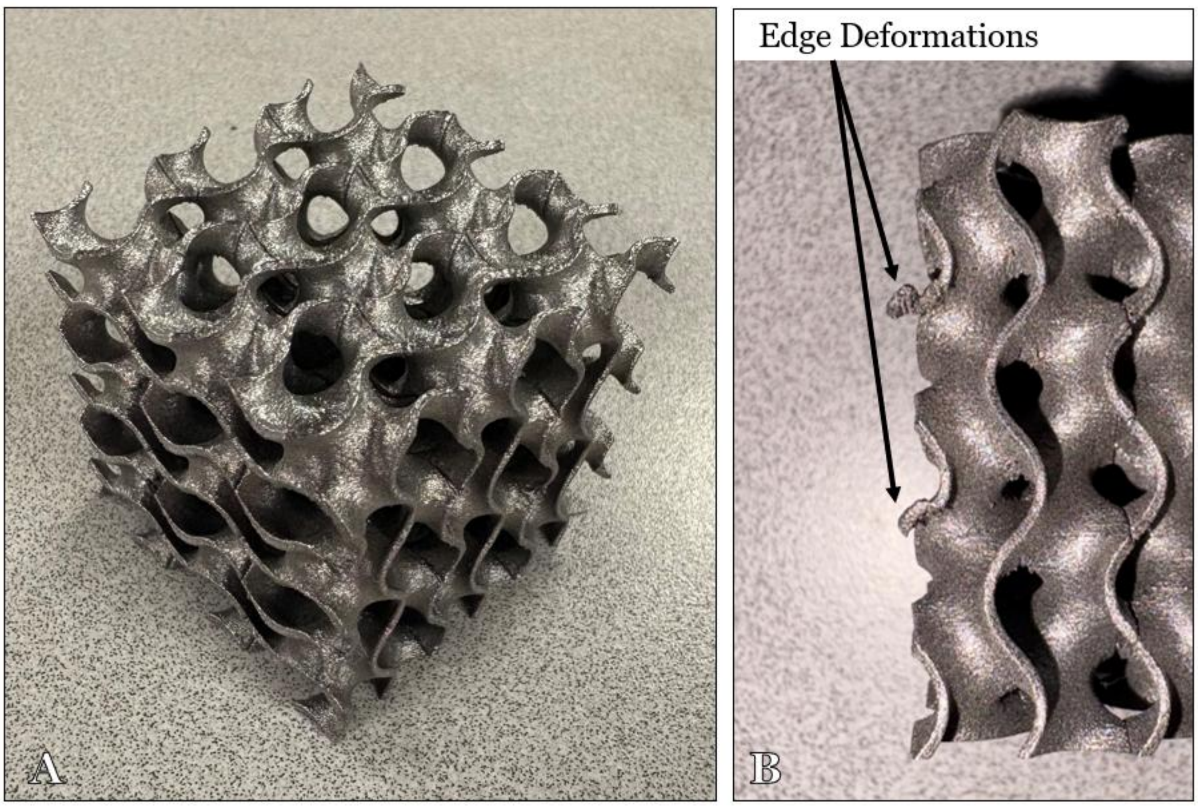

Figure 50: Stainless Steel Gyroid (a) Final Sample, and (b) Edge Deformations

The Gyroid stainless steel 17-4PH print was successful. The resolution was fine enough that a smaller thickness would be possible for future iterations, decreasing weight if needed. Furthermore, the structure itself was very stable with no immediate concerns regarding manufacturability. Overall, there was no vital problem regarding manufacturing.

There were two areas for improvement in the Gyroid stainless steel 17-4PH sample. First, there are faint lines on the sample in the location of the linear part used in the design. This was a design error and could be fixed by ensuring the sample is properly merged in SolidWorks before printing. Despite the error, the printer was still able to print the sample with gaps as small as 0.003 inches wide. The SLA printer did not have the capability to print at this resolution, further validating the resolution capabilities of the L-PBF printer. Second, there were slight deformities on the edges of the sample where it was connected to the build plate, seen in Figure 50b. This could be solved by trimming during post processing. Overall, the problems with the sample were relevantly easy to fix, meaning the Gyroid structure would be an excellent choice for L-PBF printing applications.

Chapter 6: Conclusion & Future Work

6.1 Conclusion

Additive manufacturing has allowed TPMS to be built in a relatively quick and easy manner. With the ability to print these theoretical designs in 3D applications, use for TPMS structures in industry was evaluated. Honeycomb is a common weight-reduction tool used in the aerospace industry. As such, the compressive strength of three TPMS, the Gyroid, Primitive, and Diamond, was compared to Honeycomb for aerospace applications.

The samples were sized according to ordering specifications from several Honeycomb manufacturers. The samples were each a 1.5-inch cube with side lengths of three 0.5-inch cell sizes. The thickness of the material was printed at 0.02 inches. All the designs were parameterized to ensure fast and easy adjustments. Simulations were performed on each of the samples to predict the outcome of the tests. The Diamond TPMS was eliminated due to the low contact area between each cell and the thin walls chosen based on the Honeycomb ordering websites.

The ANYCUBIC D2 SLA printer was used to print samples using standard resin. The Primitive and Honeycomb were printed using supports. The use of supports was needed because the bottom layer of each of the printers included a closed area, which would cause the print to stick to the bottom of the resin reservoir instead of the build plate. The Gyroid and Diamond samples did not have this problem because the bottom layer of the print was not a closed geometry. The Diamond samples were attempted to be printed, but like the simulations, the wall thickness and small contact area between each cell did not allow effective samples.

Five of the Gyroid and Primitive samples were printed for testing, and ten of the Honeycomb samples were printed for testing due to the need to test in both directions. The samples were tested using a 5969 Series Instron and the Zeiss Aramis Adjustable Digital Image Correlation System. These machines collected load, extension, and localized strain field as their sources of measurement. The results showed that the Honeycomb was the strongest in the axial direction with a strength-to-density ratio of 26.144, followed by the Gyroid with a ratio of 5.692. Next, the Primitive had a ratio of 5.182, and the Honeycomb Transverse had a ratio of 1.008. All ratio units were in $\frac{N}{\frac{kg}{m^3}}$.

Further consideration of entire loads paths of models would need to be computed to make a definitive statement on the ideal core structure in sandwich composites. However, as a generalization, the results show that the Gyroid is the strongest in a transverse or multi-directional load path, and Honeycomb Axial is the strongest in the uniaxial direction for load paths such as control surfaces. For applications where there in load in multiple planes, such as a truss-braced wing, the Gyroid might be a more effective option.

6.2 Future Work

To start, the use of the L-PBF printer for TPMS can be further evaluated. The successful print on the Concept Laser M2 Series 5 gave an opening for many further investigations. First, the TPMS would need to be smaller sized to be evaluated by the fifty kilonewton load cell. These smaller samples could be tested in compression, tensile, and shear. The printing of other shapes, such as airfoils, could be investigated as well.

Heat transfer through the TPMS is another area that could be investigated using the metal samples.

Tensile and shear properties of the polymer resin TPMS samples could be compared to Honeycomb as a future project. The tensile and shear directions are not considered in this report, and the TPMS may have better properties in these directions. For multi-direction loading, tensile and shear must be considered. Furthermore, the Honeycomb has a high compressive strength, so these other properties may increase the appeal for use of TPMS.

The TPMS can be used to design aerospace parts, as seen by Section 5.4. Another future project could be to design a structure for aerospace application, such as a control surface, wings truss, wing turbine, etc., using both a Honeycomb and Gyroid core, and test the application in a wind tunnel. This type of research would be an extension of the airfoil samples made in Section 3.4. Furthermore, this paper could be used as reference for compressive strength in each of the structures. Overall, TPMS can be used for multi-load applications in aerospace after the consideration of tensile and shear properties.

References

[1] H. Z. Hassan and N. M. Saeed, "Advancements and applications of lightweight structures: a comprehensive review," *Discover Civil Engineering,* vol. 1, no. 1, p. 47, 2024/08/13 2024, doi: 10.1007/s44290-024-00049-z.

[2] C. Herrmann, W. Dewulf, M. Hauschild, A. Kaluza, S. Kara, and S. Skerlos, "Life cycle engineering of lightweight structures," *CIRP Annals,* vol. 67, no. 2, pp. 651-672, 2018/01/01/ 2018, doi: https://doi.org/10.1016/j.cirp.2018.05.008.

[3] A. Ahmad, "Study on the Benefits of Lattice Structures within the Framework of High-Performance Structural Design: A Case Study," 2024.

[4] F. Nazzi, "The hexagonal shape of the honeycomb cells depends on the construction behavior of bees," *Scientific Reports,* vol. 6, no. 1, p. 28341, 2016/06/20 2016, doi: 10.1038/srep28341.

[5] N. K. Chandrasekaran and V. Arunachalam, "State-of-the-art review on honeycomb sandwich composite structures with an emphasis on filler materials," *Polymer composites.,* vol. 42, no. 10, pp. 5011-5020, 2021, doi: 10.1002/pc.26252 info:doi/10.1002/pc.26252.

[6] D. N. Ball, "Contributions of CFD to the

787 - and Future Needs," presented at the IDC HPC User Forum, Imperial College London, UK, 2008.

[7] X. Wang *et al.*, "Research on a Honeycomb Structure for Pyroshock Isolation at the Spacecraft–Rocket Interface," *Aerospace*, vol. 11, no. 9, doi: 10.3390/aerospace11090756.

[8] F. Shen and D. Pope, "Design and Development of Composite Fairing Structures for Space Launch Vehicles," *SAE Transactions,* vol. 99, pp. 1447-1455, 1990. [Online]. Available: http://www.jstor.org/stable/44473117.

[9] N. Chantarapanich *et al.*, "Fabrication of three-dimensional honeycomb structure for aeronautical applications using selective laser melting: a preliminary investigation," *Rapid prototyping journal.,* vol. 20, no. 6, pp. 551-558, 2014, doi: 10.1108/RPJ-08-2011-0086

info:doi/10.1108/RPJ-08-2011-0086.

[10] J. Pflug, B. Vangrimde, I. Verpoest, P. Bratfisch, and D. Vandepitte, "Honeycomb Core Materials: New Concepts for Continuous Production," *Sampe Journal,* vol. 39, pp. 22-30, 11/01 2003.

[11] S. David Müzel, E. P. Bonhin, N. M. Guimarães, and E. S. Guidi, "Application of the Finite Element Method in the Analysis of Composite Materials: A Review," *Polymers*, vol. 12, no. 4, doi: 10.3390/polym12040818.

[12] C. Qi, F. Jiang, and S. Yang, "Advanced honeycomb designs for improving mechanical properties: A review," *Composites Part B: Engineering,* vol. 227, p. 109393, 2021/12/15/ 2021, doi: https://doi.org/10.1016/j.compositesb.2021.109393.

[13] G. Carrier, "Investigation of a Strut-BAsed Wing Configuration for Future Commercial Transportation," *International Congress of the Aeronautical Sciences,* p. 16.

[14] E. K. Anderson, A. Cardona, and B. H. Mason, "Structural Sizing of a Composite Transonic Truss-Braced Wing," in *AIAA SCITECH 2023 Forum*, (AIAA SciTech Forum: American Institute of Aeronautics and Astronautics, 2023.

[15] K. Torabi, H. Afshari, and F. H. Aboutalebi, "Vibration and flutter analyses of cantilever trapezoidal honeycomb sandwich plates," *Journal of Sandwich Structures & Materials,* vol. 21, no. 8, pp. 2887-2920, 2019/11/01 2017, doi: 10.1177/1099636217728746.

[16] F. R. N. Nabarro, "Dislocations in a simple cubic lattice," *Proceedings of the Physical Society,* vol. 59, no. 2, p. 256, 1947/03/01 1947, doi: 10.1088/0959-5309/59/2/309.

[17] N. Thompson, "Dislocation Nodes in Face-Centred Cubic Lattices," *Proceedings of the Physical Society. Section B,* vol. 66, no. 6, p. 481, 1953/06/01 1953, doi: 10.1088/0370-1301/66/6/304.

[18] X. Ma, N. Zhang, Y. Chang, and X. Tian, "Analytical model of mechanical properties for a hierarchical lattice structure based on hierarchical body-centered cubic unit cell," *Thin-Walled Structures,* vol. 193, p. 111217, 2023/12/01/ 2023, doi: https://doi.org/10.1016/j.tws.2023.111217.

[19] B. Sherwood, C. Billings, and Y. Liu, *Parametric Modeling of Lattice Structures for Manufacturing via Masked Stereolithography Apparatus*. 2024.

[20] C. Chatzigeorgiou, B. Piotrowski, Y. Chemisky, P. Laheurte, and F. Meraghni, "Numerical investigation of the effective mechanical properties and local stress distributions of TPMS-based and strut-based lattices for biomedical applications," *Journal of the Mechanical Behavior of Biomedical Materials,* vol. 126, p. 105025, 2022/02/01/ 2022, doi: https://doi.org/10.1016/j.jmbbm.2021.105025.

[21] C. Lu, C. Zhang, P. Wen, and F. Chen, "Mechanical behavior of Al–Si10–Mg gyroid surface with variable topological parameters fabricated via laser powder bed fusion," *Journal of Materials Research and Technology,* vol. 15, pp. 5650-5661, 2021/11/01/ 2021, doi: https://doi.org/10.1016/j.jmrt.2021.11.008.

[22] W. H. Meeks, "The Theory of Triply Periodic Minimal Surfaces," *Indiana University Mathematics Journal,* vol. 39, no. 3, pp. 877-936, 1990. [Online]. Available: http://www.jstor.org/stable/24895601.

[23] C. Pan, Y. Han, and J. Lu, "Design and Optimization of Lattice Structures: A Review," *Applied Sciences*, vol. 10, no. 18, doi: 10.3390/app10186374.

[24] L. Han and S. Che, "An Overview of Materials with Triply Periodic Minimal Surfaces and Related Geometry: From Biological Structures to Self-Assembled Systems," *Advanced materials.,* vol. 30, no. 17, 2018, doi: 10.1002/adma.201705708

info:doi/10.1002/adma.201705708.

[25] M. Attaran, "The rise of 3-D printing: The advantages of additive manufacturing over traditional manufacturing," *Business Horizons,* vol. 60, no. 5, pp. 677-688, 2017/09/01/ 2017, doi: https://doi.org/10.1016/j.bushor.2017.05.011.

[26] J. Borrello, P. Nasser, J. C. Iatridis, and K. D. Costa, "3D printing a mechanically-tunable acrylate resin on a commercial DLP-SLA printer," *Additive Manufacturing,* vol. 23, pp. 374-380, 2018/10/01/ 2018, doi: https://doi.org/10.1016/j.addma.2018.08.019.

[27] P. Robles Martinez, A. W. Basit, and S. Gaisford, "The History, Developments and Opportunities of Stereolithography," in *3D Printing of Pharmaceuticals*, A. W. Basit and S. Gaisford Eds. Cham: Springer International Publishing, 2018, pp. 55-79.

[28] G. Singh, "Exploring the Evolution, Applications, Materials, and Sustainability of 3D Printing Technology in the Manufacturing Sector," *International Journal of Innovative Research in Science and Engineering,* vol. 10, no. 02, p. 8, 2024 2024.

[29] M. M. Ahsan, Y. Liu, S. Raman, and Z. Siddique, "Digital Twins in Additive Manufacturing: A Systematic Review," *arXiv preprint arXiv:2409.00877,* 2024.

[30] S. H. Ahn, M. Montero, D. Odell, S. Roundy, and P. K. Wright, "Anisotropic material properties of fused deposition modeling ABS," *Rapid Prototyping Journal,* vol. 8, no. 4, pp. 248-257, 2002, doi: 10.1108/13552540210441166.

[31] R. Villa, Y. Liu, and Z. Siddique, "Review of defects and their sources in as-built Ti6Al4V manufactured via powder bed fusion," *The International Journal of*

Advanced Manufacturing Technology, vol. 132, no. 9, pp. 4105-4134, 2024/06/01 2024, doi: 10.1007/s00170-024-13611-x.

[32] E. De Leon, A. Riensche, B. D. Bevans, C. Billings, Z. Siddique, and Y. Liu, "A Review of Modeling, Simulation, and Process Qualification of Additively Manufactured Metal Components via the Laser Powder Bed Fusion Method," *Journal of Manufacturing and Materials Processing*, vol. 9, no. 1, doi: 10.3390/jmmp9010022.

[33] G. K. Maharjan, "Compressive Behavior of 3D Printed Polymeric Gyroid Cellular Structure," *Matierals Science and Engineering,* 2018.

[34] G. Guimarães, A. Rocha, R. Rego, L. Barreiros, J. Mascheroni, and A. Kretzer, "Compressive Behavior of Gyroid Structures Manufactured Through SLM with Carburizing Steels: A Numerical and Experimental Study," *Procedia Structural Integrity,* vol. 34, pp. 26-31, 2021/01/01/ 2021, doi: https://doi.org/10.1016/j.prostr.2021.12.004.

[35] D. W. Abueidda, M. Elhebeary, C.-S. Shiang, S. Pang, R. K. Abu Al-Rub, and I. M. Jasiuk, "Mechanical properties of 3D printed polymeric Gyroid cellular structures: Experimental and finite element study," *Materials & Design,* vol. 165, p. 107597, 2019/03/05/ 2019, doi: https://doi.org/10.1016/j.matdes.2019.107597.

[36] X. Guo *et al.*, "Enhancement in the mechanical behaviour of a Schwarz Primitive periodic minimal surface lattice structure design," *International Journal of*

Mechanical Sciences, vol. 216, p. 106977, 2022/02/15/ 2022, doi: https://doi.org/10.1016/j.ijmecsci.2021.106977.

[37] J. Maszybrocka, B. Gapiński, M. Dworak, G. Skrabalak, and A. Stwora, "The manufacturability and compression properties of the Schwarz Diamond type Ti6Al4V cellular lattice fabricated by selective laser melting," *The International Journal of Advanced Manufacturing Technology,* vol. 105, no. 7, pp. 3411-3425, 2019/12/01 2019, doi: 10.1007/s00170-019-04422-6.

[38] M. A.-O. Saleh, S. A.-O. X. Anwar, A. A.-O. Al-Ahmari, and A. A.-O. Alfaify, "Compression Performance and Failure Analysis of 3D-Printed Carbon Fiber/PLA Composite TPMS Lattice Structures. LID - 10.3390/polym14214595 [doi] LID - 4595," (in eng), no. 2073-4360 (Electronic).

[39] H. Niknam and A. H. Akbarzadeh, "Graded lattice structures: Simultaneous enhancement in stiffness and energy absorption," *Materials & Design,* vol. 196, p. 109129, 2020/11/01/ 2020, doi: https://doi.org/10.1016/j.matdes.2020.109129.

[40] S. Saseendran, M. Wysocki, and J. Varna, "Cure-state dependent viscoelastic Poisson's ratio of LY5052 epoxy resin," *Advanced Manufacturing: Polymer & Composites Science,* vol. 3, no. 3, pp. 92-100, 2017/07/03 2017, doi: 10.1080/20550340.2017.1348002.

[41] B. C. Yemineni, J. Mahendra, J. Nasina, L. Mahendra, L. Shivasubramanian, and S. B. Perika, "Evaluation of Maximum Principal Stress, Von Mises Stress, and

Deformation on Surrounding Mandibular Bone During Insertion of an Implant: A Three-Dimensional Finite Element Study," (in eng), no. 2168-8184 (Print).

[42] R. Patel *et al.*, "A Transdisciplinary Approach for Analyzing Stress Flow Patterns in Biostructures," *Mathematical and Computational Applications,* vol. 24, p. 47, 04/26 2019, doi: 10.3390/mca24020047.

[43] C. Nguyen and A. B. Kamaraj, "Impact of lattice structure on compressive performance and strength to weight ratio in continuous stereolithography," *Manufacturing Letters,* vol. 41, pp. 998-1003, 2024/10/01/ 2024, doi: https://doi.org/10.1016/j.mfglet.2024.09.124.